

Comparative Study of State-of-the-Art Matrix-Product-State Methods for Lattice Models with Large Local Hilbert Spaces

**J Stolpp¹, T Köhler², S R Manmana¹, E Jeckelmann³,
F Heidrich-Meisner¹ and S Paeckel⁴**

¹ Institut für Theoretische Physik, Georg-August-Universität Göttingen, 37077 Göttingen, Germany

² Department of Physics and Astronomy, Uppsala University, Box 516, S-751 20 Uppsala, Sweden

³ Leibniz Universität Hannover, Institut für Theoretische Physik, 30167 Hannover, Germany

⁴ Department of Physics, Arnold Sommerfeld Center for Theoretical Physics (ASC), Munich Center for Quantum Science and Technology (MCQST), Ludwig-Maximilians-Universität München, 80333 München, Germany

E-mail: sebastian.paeckel@physik.uni-muenchen.de

Abstract. Lattice models consisting of high-dimensional local degrees of freedom without global particle-number conservation constitute an important problem class in the field of strongly correlated quantum many-body systems. For instance, they are realized in electron-phonon models, cavities, atom-molecule resonance models, or superconductors. In general, these systems elude a complete analytical treatment and need to be studied using numerical methods where matrix-product states (MPS) provide a flexible and generic ansatz class. Typically, MPS algorithms scale at least quadratic in the dimension of the local Hilbert spaces. Hence, tailored methods, which truncate this dimension, are required to allow for efficient simulations. Here, we describe and compare three state-of-the-art MPS methods each of which exploits a different approach to tackle the computational complexity. We analyze the properties of these methods for the example of the Holstein model, performing high-precision calculations as well as a finite-size-scaling analysis of relevant ground-state observables. The calculations are performed at different points in the phase diagram yielding a comprehensive picture of the different approaches.

1. Introduction

In the past two decades, tensor-network state (TNS) based methods have become very successful tools to study strongly correlated, low-dimensional quantum systems in and out of equilibrium [1–7]. In principle, these methods can reach a very high accuracy and are in many ways unbiased and flexible. Re-expressing the early algorithms of the density-matrix renormalization group (DMRG) [1, 2] using matrix-product state (MPS) [3, 8] representations paved the way for the formulation of efficient and flexible variational algorithms to study correlated quantum systems with excellent precision in one dimension [5, 6, 9, 10]. Exploring the tensor-product structure of the many-body Hilbert space to decompose the coefficients of a quantum state into *local* tensors yields a powerful formulation of DMRG and allows the exploitation of ideas from quantum-information theory [5, 11, 12]. Thereby, numerical optimization schemes that work on the local tensors can be formulated, which is at the heart of their high efficiency.

Unfortunately, such a decomposition becomes numerically very costly if the local quantum systems have a large number of internal degrees of freedom that do not obey conservation laws. Indeed, these situations are not too exotic as may be illustrated by the simple example of lattice fermions locally coupled to Einstein phonons, the Holstein model [13]. Describing such a system by means of MPS requires, in principle, an infinite number of local degrees of freedom, while in practice, one needs to introduce a cutoff in the local Hilbert space dimension [14, 15]. As is well known, these systems can feature rich physics. Modeling the influence of phonons on interacting fermions on a numerically unbiased footing [16–22] is an important problem with many intensively studied questions, such as the formation, stability, and dynamics of (bi-)polarons in the (Hubbard-)Holstein model [23–30]. Various numerical approaches have been employed to study these systems ranging from exact diagonalization [31, 32] over quantum Monte-Carlo methods [33, 34] to dynamical mean-field theory (DMFT) [35–37].

Ultracold atoms provide another relevant platform in which large local Hilbert spaces play an important role for the theoretical description. For instance, models involving Feshbach-resonances feature a molecular and an atomic channel as well as a term that converts two atoms into one molecule. As a consequence, the particle numbers of molecules and atoms are not conserved individually. These models are called Bose-Fermi or Bose-Bose resonance models [38–41]. Models of single atoms coupled to optical cavities [42–44] have to account for the bosonic nature of the light field and are important systems to understand the interplay between light and matter on the atomic scale. Finally, in heterostructures of proximity-coupled s-wave superconductors, the condensate can be described separately, yielding an effective bosonic bath with pairwise creation and annihilation of particles. Recently, these systems have been suggested as promising candidates for an experimental realization of Majorana quasi particles, potential building blocks of topological qubits [45–48].

Here, we discuss three state-of-the-art MPS methods that can be utilized to efficiently deal with such a large number of required local degrees of freedom: The

pseudosite DMRG (PS-DMRG) method [23], DMRG with local basis optimization (DMRG-LBO) [26, 49–52], and the projected purified two-site DMRG (PP-2DMRG) [53]. The first method was introduced by Jeckelmann and White to extend the applicability of DMRG to describe electrons coupled to phonons [23]. Local basis optimization (LBO) proposed by Zhang *et al.* [49] is based on a rotation into the eigenbasis of the single-site reduced density matrix. It allows for a faithful truncation yielding an optimal approximation of the single-site reduced density matrix. The PP-2DMRG developed recently by some of the authors consists of a mapping of the initial problem into a purified Hilbert space with a subsequent projection into an invariant subspace to generate an artificial $U(1)$ symmetry that collapses the local dimensions of the bosonic degrees of freedom and allows to exploit canonical MPS truncation schemes [53].

We compare the methods by applying them to the Holstein model at half filling. This system undergoes a phase transition from a gapless Luttinger-liquid (LL) phase to a gapped charge-density wave (CDW) phase upon changing the electron-phonon coupling [18, 54–56]. To this end, we conduct high-precision calculations at an intermediate system size of $L = 51$ (where L is the number of sites) and perform a finite-size extrapolation of the ground-state energy and the CDW order parameter from data at $L = 51, 101, 151, 201$ with relaxed precision demands. According to our analysis, all three methods agree within their anticipated error margins. We further find that the PS-DMRG and the PP-2DMRG require a larger bond dimension in order to reach a comparable precision as DMRG-LBO. However, the efficient representation of states using the DMRG-LBO method comes at the cost of additional numerical control parameters in which the calculations have to be converged. Here, the PS-DMRG and PP-2DMRG benefit from being conceptually simpler approaches. PS-DMRG can be converged with respect to a scaling analysis in the bond dimension and comparative calculations using different local Hilbert-space dimensions. Finally, using PP-2DMRG, it suffices to converge the calculations in the discarded weight, only. On the one hand, this comes at the cost of the largest growth in bond dimension compared to the other methods, but, on the other hand, this can be compensated by exploiting the restored global $U(1)$ symmetries.

The paper is organized as follows: In section 1.1, we briefly review the Holstein model and its phase diagram at half filling. In section 2, we introduce the different numerical methods. After recapitulating some basic facts about MPSs in section 2.1, we introduce the PS-DMRG in section 2.2, the strictly single-site DMRG with LBO (DMRG3S+LBO) in section 2.3, and the PP-2DMRG in section 2.4. Section 3 is devoted to the comparison between the methods, where section 3.1 and section 3.2 contain the high-precision calculations, while section 3.3 contains the finite-size extrapolations. Finally, in section 4, we give a conclusion of our work.

1.1. Holstein Model

In order to demonstrate the applicability of the different methods, we conduct numerical ground-state calculations of the half-filled 1D Holstein model with spinless fermions [13]. The model is defined by a set of spinless fermions with creation/annihilation operators $\hat{c}_j^{[\dagger]}$ on a lattice, where every lattice site possesses an associated harmonic oscillator with bosonic creation/annihilation operators $\hat{b}_j^{[\dagger]}$. The oscillators are decoupled from each other and play the role of a single Einstein-phonon branch. The density of the fermions $\hat{n}_j^f = \hat{c}_j^\dagger \hat{c}_j$ at a specific site j couples to the displacement $(\hat{b}_j^\dagger + \hat{b}_j)$ of the associated harmonic oscillator:

$$\hat{H} = \hat{H}_f + \hat{H}_{ph} + \hat{H}_{f-ph} \quad (1)$$

$$\hat{H}_f = -t_0 \sum_j \left(\hat{c}_j^\dagger \hat{c}_{j+1} + \text{h.c.} \right) \quad (2)$$

$$\hat{H}_{ph} = \omega_0 \sum_j \hat{b}_j^\dagger \hat{b}_j \quad (3)$$

$$\hat{H}_{f-ph} = \gamma \sum_j \hat{n}_j^f \left(\hat{b}_j^\dagger + \hat{b}_j \right) . \quad (4)$$

An important exact relation between the different particle species and for eigenstates is given by [54, 57]

$$\langle \hat{b}_j^\dagger + \hat{b}_j \rangle = 2 \frac{\gamma}{\omega_0} \langle \hat{n}_j^f \rangle . \quad (5)$$

At half filling, the ground-state phase diagram of this model exhibits a transition from a metallic LL phase into a CDW insulating phase when increasing the ratio γ/t_0 for fixed $t_0/\omega_0 \neq 0$ [18, 54–56] (see figure 1).

We investigate the Holstein model with open boundary conditions at different points in its parameter space. In particular, we choose the following sets of parameters

$$\omega_0/t_0 = 1.0, \quad \gamma/t_0 = 0.5 , \quad (\text{P.1})$$

$$\omega_0/t_0 = 1.0, \quad \gamma/t_0 = 1.5 , \quad (\text{P.2})$$

$$\omega_0/t_0 = 1.0, \quad \gamma/t_0 = 2.0 , \quad (\text{P.3})$$

so that we expect the ground state to realize a LL for the parameter set (P.1), (P.2) is close to the phase boundary, and a CDW is realized for (P.3) (cf., figure 1).

An important aspect is the absence of particle-number conservation in the phonon system. As a consequence, techniques to decompose tensors into irreducible representations with respect to global $U(1)$ -symmetries [58–60] cannot be applied to the phononic degrees of freedom in order to reduce the numerical complexity. Combined with the large dimension of the local Hilbert spaces, this paradigmatic model is surprisingly challenging for standard MPS methods and specialized algorithms have to be utilized, which are discussed in the next section.

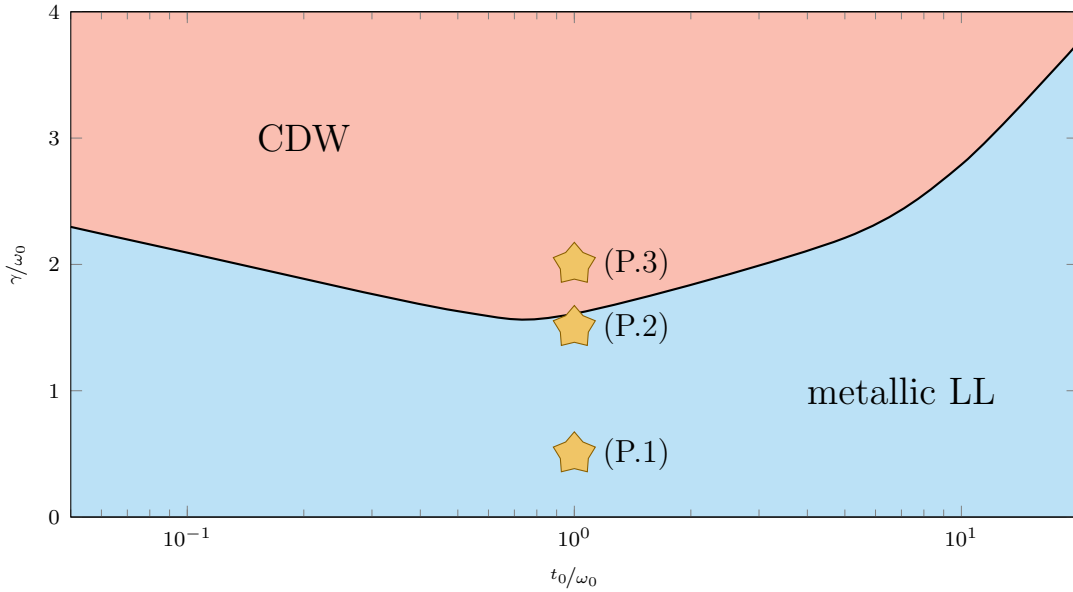


Figure 1. Schematic reproduction of the phase diagram of the 1D Holstein model computed in [55]. The transition between the CDW and the metallic LL phase is controlled by the coupling γ between the local oscillator displacement and the fermion density as well as the phonon frequency ω_0 . Marked points indicate the position of the parameter sets studied in this paper.

2. Methods

The numerical efficiency of the MPS representation is rooted in the fact that in one dimension, they efficiently parameterize so-called area-law states. Therein, the entanglement entropy

$$S_N = -\text{Tr} \{ \hat{\rho}_{A/B} \log (\rho_{A/B}) \} \quad (6)$$

scales only with the surface area of the partitioned subsystems [61]. For instance, for gapped one-dimensional (1D) systems, S_N is bounded by a constant. Here, $\rho_{A/B}$ is the reduced density matrix of a bipartition of the many-particle Hilbert space $\mathcal{H} = \mathcal{H}_A \otimes \mathcal{H}_B$. There has been great effort to characterize the entanglement properties of generic models and it has been shown that for a wide range of gapped systems with local couplings, the ground states obey the area law and thus can be represented efficiently using MPS [62–64].

For pure fermion or small-spin systems, the dominating numerical costs are caused by contracting the site tensors along the auxiliary index between two lattice sites. However, in typical algorithms such as a ground-state search, the local dimension d enters the numerical complexity as d^2 or d^3 in case of a single- or two-site algorithm [6, 65]. Therefore, a generic representation allowing to numerically treat large d values is essential, particularly in the intermediate coupling regime. A loophole is to exploit global $U(1)$ symmetries, decomposing the local degrees of freedom into 1D

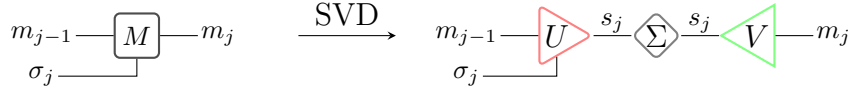


Figure 2. SVD of a site tensor M into a right orthonormal tensor U (red triangle), a diagonal matrix Σ (grey diamond), and a left orthonormal tensor V (green triangle). This operation is used to bring a site tensor M into left canonical form via setting $A_{m_{j-1},m_j}^{\sigma_j} = U_{(\sigma_j, m_{j-1}), s_j}$ and contracting Σ and V with the following site tensor.

representations [58, 60]. However, in the Holstein model, the number of phonons is not conserved, which is one major reason for the numerically challenging situation.

2.1. Matrix-Product States

MPSs supply both a flexible and numerically efficient ansatz class for quantum many-body states. The coefficients $\psi_{\sigma_1, \dots, \sigma_L} \in \mathbb{C}$ of a wave function representing a state $|\psi\rangle \in \mathcal{H}$ in a Hilbert space \mathcal{H} composed of the tensor product of $L \in \mathbb{N}$ d -dimensional local degrees of freedom are expanded in terms of $d \cdot L$ matrices $M^{\sigma_j} \in \mathbb{C}^{m_{j-1} \times m_j}$ [6]

$$|\psi\rangle = \sum_{\sigma_1, \dots, \sigma_L} \psi_{\sigma_1, \dots, \sigma_L} |\sigma_1, \dots, \sigma_L\rangle \equiv \sum_{\sigma_1, \dots, \sigma_L} M^{\sigma_1} \cdots M^{\sigma_L} |\sigma_1, \dots, \sigma_L\rangle. \quad (7)$$

Encoding the information of the wave function locally in rank 3 site tensors M_j (i.e., the set of matrices $\{M^{\sigma_j}\}$ per site) provides direct access to the Schmidt coefficients if the site tensors are expressed in the canonical gauge [6]. Site tensors A_j are called left canonical if they fulfill $\sum_{\sigma_j, m_{j-1}} (A_{m_{j-1}, m_j}^{\sigma_j})^\dagger A_{m_{j-1}, m_j}^{\sigma_j} = 1_{m_j, m_j}$ and site tensors B_j are called right canonical if they fulfill $\sum_{\sigma_j, m_j} B_{m_{j-1}, m_j}^{\sigma_j} (B_{m_{j-1}, m_j}^{\sigma_j})^\dagger = 1_{m_{j-1}, m_{j-1}}$. The singular-value decomposition (SVD) is one way of obtaining these canonical tensors (see figure 2).

Expanding the site tensors of a canonically gauged state by means of a SVD

$$M^{\sigma_j} = M_{(\sigma_j, m_{j-1}), m_j} = \sum_{s_j} U_{(\sigma_j, m_{j-1}), s_j} \Sigma_{s_j} V_{s_j, m_j} \quad (8)$$

allows for an optimal approximation with respect to the reduced density matrix $\hat{\rho} = \text{Tr}_{k \leq j} |\psi\rangle \langle \psi|$ by truncating the series of Schmidt values Σ_{s_j} below a certain threshold δ_0 , leading to a cutoff bond dimension m_{\max} . The squared and summed discarded parts of the Schmidt spectrum are commonly referred to as discarded weight $\delta(m_{\max})$

$$\delta = \sum_{s_j > m_{\max}} \Sigma_{s_j}^2. \quad (9)$$

Rapidly decaying Schmidt values Σ_{s_j} are thus a necessary condition for a compact approximation of a state by means of a MPS and small truncation error controlled by δ .

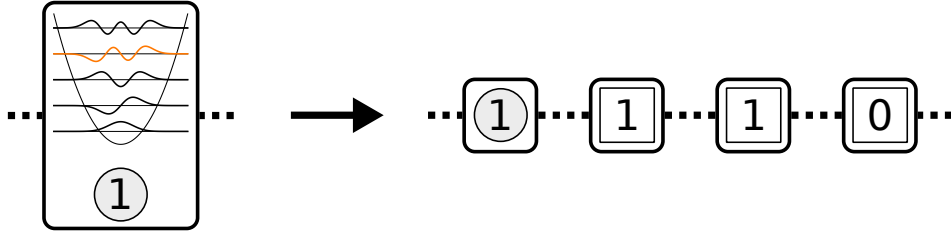


Figure 3. Sketch of local Hilbert space unfolded into pseudosites encoding n_{pseudo} local degrees of freedom. Using a binary number representation, the local dimension is $2^{n_{\text{pseudo}}} - 1$. The fermionic degree of freedom is indicated by a circle while the squares denote the introduced pseudo sites.

Further numerical benefits can be achieved if $|\psi\rangle$ transforms under a global symmetry group G . In this situation, the Wigner-Eckhardt theorem ensures a decomposition of the site tensors in terms of irreducible representations $\Gamma(g)$ of the elements in the symmetry group $g \in G$ [58–60]. The dimensions of the tensor indices decompose under the action of G : $m_j = \sum_{g_j} m_{g_j}$ so that by working on each block separately, the computational costs typically are reduced by an order of magnitude in the case of a global $U(1)$ symmetry.

2.2. Pseudosite Method

In this section, we summarize the PS-DMRG method for large local dimensions d . Details can be found in [23, 31]. The pseudosite approach is based on the original two-site DMRG method [1, 2]. Without special techniques for large sites, the complexity of the two-site DMRG method scales as $SLd^3m_{\text{max}}^3$, where L is the number of sites in the lattice and m_{max} is the maximum bond dimension. In the spinless Holstein model, $d = 2(n_{\text{ph}} + 1)$, where n_{ph} is the maximum number of phonons per site. S represents the number of iterations required to achieve convergence and combines both the iterative diagonalization of the superblock Hamiltonian at each DMRG step and the repeated DMRG sweeps through the lattice.

The key idea of the PS-DMRG method is to substitute $n_{\text{pseudo}} = \log_2(n_{\text{ph}} + 1)$ pseudosites of dimension 2 for the phonon site of dimension $n_{\text{ph}} + 1$. As the computational cost increases linearly with the number of sites but with the cube of the site dimension, PS-DMRG can handle this representation more efficiently. The exact mapping between the truncated phonon Hilbert space and the Hilbert space spanned by the n_{pseudo} pseudosites can be implemented using the binary number representation of the boson number n ($0 \leq n \leq n_{\text{ph}}$) on a site. An occupied pseudosite corresponds to the binary digit 1 while an empty pseudosite corresponds to the binary digit 0 (cf., figure 3). Boson operators have to be represented in terms of pseudosite operators to perform PS-DMRG calculations.

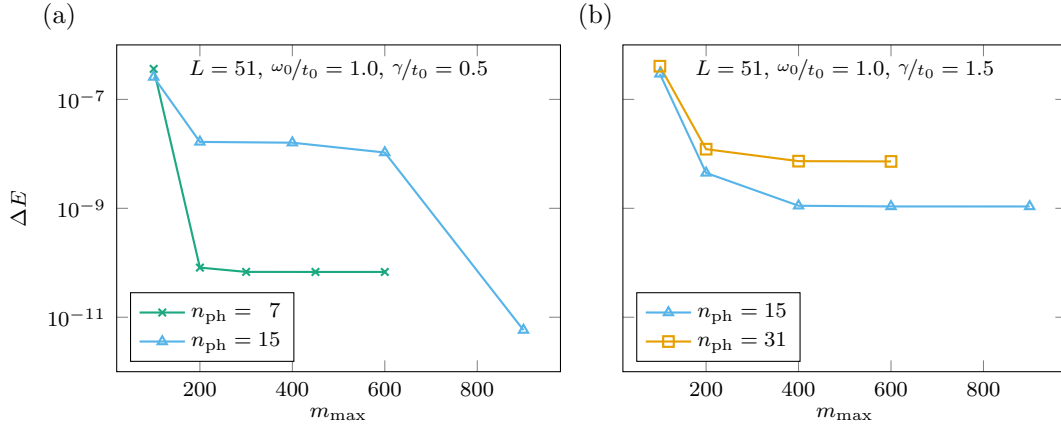


Figure 4. Relative deviation of the ground-state energy obtained with PS-DMRG from the smallest value obtained in the high-precision calculations in section 3.1 as a function of the maximum bond dimension m_{\max} and varying phonon cutoff n_{ph} .

2.2.1. Number of Pseudosites For the Holstein model, the pseudosite Hamiltonian contains $\sim n_{\text{ph}}$ many-particle terms acting over a range of up to n_{pseudo} pseudosites. Thus, the computational cost of the PS-DMRG method scales as $SL(n_{\text{ph}}+1) \log_2(n_{\text{ph}}+1)m_{\max}^3$, which is significantly more efficient than the usual DMRG method applied to large phonon sites. Due to the longer interaction range in the pseudosite representation, however, the PS-DMRG method requires a larger bond dimension m_{\max} and a larger number of iterations S to reach a given accuracy. The difference becomes more pronounced for larger site dimensions. Thus, the precision increases first with increasing the number of pseudosites, but may deteriorate for too large n_{pseudo} if the number of sweeps and the bond dimension are kept constant, as observed in figure 4(b). Nonetheless, the PS-DMRG method allows much larger numbers of bosons than the usual DMRG method [66–68]. It was successfully used to study the metal-insulator transition in various Holstein-type models [14, 57, 69–71].

2.2.2. Benchmark Setup For the high-precision calculations presented in section 3.1, we use n_{pseudo} from 3 to 6 ($7 \leq n_{\text{ph}} \leq 63$). The PS-DMRG calculation always starts with a small bond dimension m , which is increased progressively up to m_{\max} . Three to six DMRG sweeps (back and forth) through the full lattice are carried out for each bond dimension for a total of up to 30 sweeps. The bond dimensions are so large that the discarded weight δ vanishes within the machine precision (10^{-16}). Thus δ is not a helpful quantity to decide whether a calculation has converged and extrapolations of observables to vanishing discarded weights are not used [31]. The accuracy of the calculated energies is limited by the slow convergence with the number of iterations rather than by the DMRG truncation error or the phonon Hilbert-space truncation.

For the study of the finite-size scaling of the order parameter in section 3.3, we use several bond dimensions m up to $m_{\max} = 200$ or 400 with 3 to 6 sweeps for each value

of m . From the scaling with varying bond dimension m , we estimate the relative errors of the finite-system energies to be smaller than 10^{-6} , while the absolute errors of the finite-system order parameters are smaller than 10^{-5} .

2.3. DMRG with local basis optimization

Here, we recapitulate the DMRG3S+LBO introduced in [30] (see also [72]). The method is based on the LBO introduced by Zhang *et al.* [49]. At the core, the DMRG3S+LBO is a combination of the variational matrix-product state (VMPS) method originally formulated for spin-boson models and introduced by Guo *et al.* [73] (see also [74–76]) with the single-site DMRG method with subspace expansion introduced by Hubig *et al.* [65].

2.3.1. LBO The LBO tackles the problem of large local Hilbert spaces by dynamically finding an optimized local basis for the problem at hand. The optimized basis at site j can be found by computing the single-site reduced density matrix:

$$\hat{\rho}_j = \text{Tr}_{k \neq j} |\psi\rangle \langle \psi| , \quad (10)$$

where the trace is over all degrees of freedom σ_k that are not on site j . Upon diagonalization of $\hat{\rho}_j$, a local basis transformation matrix U_l as well as the spectrum of $\hat{\rho}_j$ is found. Along the lines of the DMRG strategy, the local basis can be truncated according to the spectrum of $\hat{\rho}_j$ and the state can be transformed into the new local basis. If only a few of the eigenvalues of $\hat{\rho}_j$ have considerable magnitude, the truncation will retain most of the information in the state. In case of the Holstein model, this strategy can be motivated by the insight that the ground state of the Holstein model in the atomic limit ($t_0 = 0$) needs just a single state at every site [54]. In the ground state of the Holstein-polaron model, an exponential decay of the spectrum was found numerically for several sets of parameters [49, 77]. A similar behavior in the spectrum of $\hat{\rho}_j$ was also found in the Bose-Bose resonance model [41].

A MPS with LBO takes the form:

$$|\psi\rangle \approx \sum_{\substack{\sigma_1, \dots, \sigma_L \\ \tilde{\sigma}_1, \dots, \tilde{\sigma}_L}} M^{\tilde{\sigma}_1} R^{\tilde{\sigma}_1, \sigma_1} \dots M^{\tilde{\sigma}_L} R^{\tilde{\sigma}_L, \sigma_L} |\sigma_1, \dots, \sigma_L\rangle , \quad (11)$$

where truncated local basis transformations R_j (with entries $R^{\tilde{\sigma}_j, \sigma_j}$) are attached to every local tensor M_j (i.e., the set of matrices $\{M^{\tilde{\sigma}_j}\}$) (cf., figure 5 left). The matrices R_j have dimension $d_o \times d$, where d_o is the number of optimal modes, i.e., the number of local basis states that are kept after the truncation.

2.3.2. DMRG3S+LBO The DMRG3S+LBO method consists of two stages, an optimization of the local basis matrix R_j and an optimization of the local site tensor M_j . Both of these are performed by a DMRG-like optimization step. The tensor

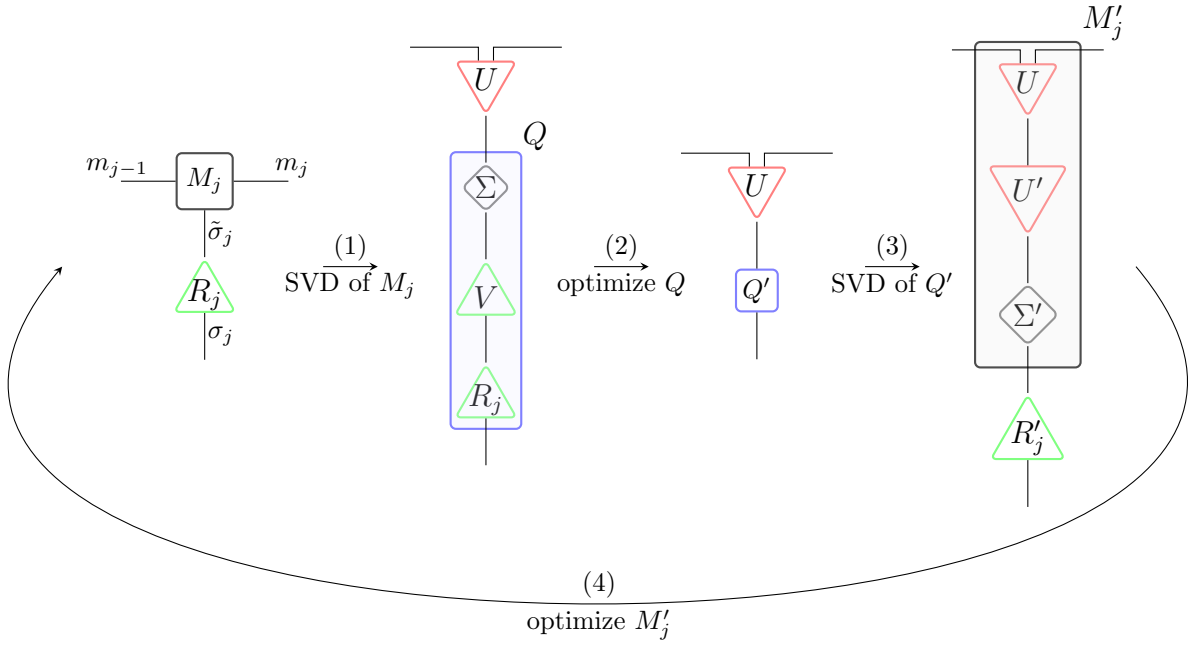


Figure 5. Sketch of the different steps in the DMRG3S+LBO method to optimize the local basis matrix R_j and the local site tensor M_j (see also [30, 73]).

manipulations necessary are sketched in figure 5. Consider a MPS with LBO in mixed-canonical form where all site tensors left of site j are left canonical and all tensors to the right are right canonical. In the first step, a SVD of the site tensor is performed such that [cf., figure 5(1)]:

$$M_{(m_{j-1}, m_j), \tilde{\sigma}_j} = \sum_{s_j} U_{(m_{j-1}, m_j), s_j} \Sigma_{s_j} V_{s_j, \tilde{\sigma}_j} . \quad (12)$$

Subsequently, Σ and V are contracted with R_j and a DMRG optimization of the resulting matrix is performed [cf., figure 5(2)]. The original form of the MPS is then restored by a SVD of the optimized matrix [cf., figure 5(3)]. In this step, a truncation of the optimal basis may be done. However, note that the optimized basis dimension cannot grow throughout the optimization step. A truncation is therefore only necessary if the left dimension of the matrix R_j is larger than the desired d_o before the optimization. In practice, it is more common that the dimension has to be enlarged artificially (e.g., in the first sweep if the initial state has a simple structure) so that future optimization steps can explore the full d_o local states. Note further that we utilize particle-number conservation of the fermions in the Holstein model so that the local-basis-transformation matrices consist of two symmetry blocks. The maximal number of optimal modes d_o refers to the maximal number per block. In the truncation step, the singular values from both blocks are combined in one list and the blocks are filled according to the size of the singular values until one of the blocks reaches the maximal size d_o . The smaller block is then filled with zeros so that both blocks have the same size.

The second step is a DMRG optimization of the local site tensor M_j [cf., figure 5(4)].

These two steps of optimizing the local basis and then the site tensor can be done in a loop until no further improvements are detected [73]. However, in the implementation of the DMRG3S+LBO algorithm used for this work, every optimization is done for a fixed number of two times.

After the optimization of both, the local basis and the site tensor is finished, the center of the mixed-canonical MPS is moved to the next site. To prevent the algorithm from getting stuck in local minima of the energy landscape, an enrichment step on the bonds has to be implemented. For this purpose, the subspace expansion described in [65] is used.

2.3.3. Convergence of the DMRG3S+LBO method In a single-site DMRG method, the bond dimension does not grow on its own during the algorithm. Therefore, it is crucial to implement a procedure that enhances the bond dimension artificially. This procedure has the second purpose of preventing the algorithm from getting stuck in local energy minima. In the DMRG3S+LBO, we choose the subspace expansion developed by Hubig *et al.* in [65] (see also [58, 78] for earlier work on single-site DMRG algorithms). The crucial steps of the method are recapitulated here. In a left-to-right sweep, after the DMRG optimization of the local tensor M_j , the tensor is enlarged by P_j with entries:

$$P_{k_{j-1},(l_j,m_j)}^{\tilde{\sigma}'_j} = \alpha \sum_{l_{j-1},m_{j-1},\tilde{\sigma}_j} L_{k_{j-1},l_{j-1},m_{j-1}} M_{m_{j-1},m_j}^{\tilde{\sigma}_j} H_{l_{j-1},l_j}^{\tilde{\sigma}_j, \tilde{\sigma}'_j}, \quad (13)$$

where H_j (with entries $H_{l_{j-1},l_j}^{\tilde{\sigma}_j, \tilde{\sigma}'_j}$) is the local matrix-product operator (MPO) site tensor of the Hamiltonian transformed into the optimal basis:

$$H_{l_{j-1},l_j}^{\tilde{\sigma}_j, \tilde{\sigma}'_j} = \sum_{\sigma_j, \sigma'_j} R^{\tilde{\sigma}_j, \sigma_j} H_{l_{j-1},l_j}^{\sigma_j, \sigma'_j} (R^\dagger)^{\sigma'_j, \tilde{\sigma}'_j} \quad (14)$$

and the tensor L_{j-1} is recursively defined as having entries:

$$L_{k_{j-1},l_{j-1},m_{j-1}} = \sum_{k_{j-2},l_{j-2},m_{j-2},\tilde{\sigma}_{j-1},\tilde{\sigma}'_{j-1}} L_{k_{j-2},l_{j-2},m_{j-2}} A_{m_{j-2},m_{j-1}}^{\tilde{\sigma}_{j-1}} H_{l_{j-2},l_{j-1}}^{\tilde{\sigma}_{j-1}, \tilde{\sigma}'_{j-1}} (A^\dagger)_{k_{j-2},k_{j-1}}^{\tilde{\sigma}'_{j-1}}, \quad (15)$$

where the A_j are the left-canonical site tensors of the MPS and $L_0 = 1$. The parameter α is a mixing factor that has to be chosen appropriately. The tensor on site j is enlarged by P_j and the MPS tensor on the following site $j+1$ is enlarged by zeros in such a way that the tensors fit together:

$$\tilde{M}_j = [M_j P_j], \quad \tilde{B}_{j+1} = \begin{bmatrix} B_{j+1} \\ 0 \end{bmatrix}. \quad (16)$$

The previous step of enlarging the tensor M_j by P_j does not change the state at all, since the expansion tensor P_j is multiplied by zeros on the next site. However, the bond dimension between site j and $j+1$ is increased by $w \cdot \chi$, where w is the bond

dimension of the MPO and χ is the bond dimension of the MPS. In most cases, it is therefore necessary to truncate the bond dimension to the maximal bond dimension m_{\max} immediately after the enrichment step. After the truncation, the change done to the state becomes manifest and in most cases, the subspace enlargement and subsequent truncation increases the energy. To monitor the effect of the subspace expansion on the state, one compares the energy after the truncation on the last bond E_{last} with the energy after the DMRG optimization on the current site E_{opt} and the energy after the truncation on the current bond E_{trunc} . This provides the energy differences $\Delta_{\text{opt}} = E_{\text{last}} - E_{\text{opt}}$ and $\Delta_{\text{trunc}} = E_{\text{trunc}} - E_{\text{opt}}$. On the one hand, it is, of course, important to keep $\Delta_{\text{opt}} > \Delta_{\text{trunc}}$, as otherwise the energy actually grows and one does not approach the ground state. On the other hand, one has to apply a strong enough mixing so that the global energy minimum can be found.

As suggested in [65], we update the mixing factor with a multiplicative adaption factor η such that $\alpha' = \eta\alpha$. The overall strategy is to increase the mixing factor if the ratio $\Delta_{\text{trunc}}/\Delta_{\text{opt}}$ is very small (or even negative) but to decrease it if the ratio exceeds 0.3. The exact procedure to choose the adaption factor η is given in algorithm 1.

Algorithm 1 Procedure to choose the adaption factor η for the update of the mixing factor α from the energy differences Δ_{opt} and Δ_{trunc} .

```

 $\delta_{\text{opt}} = \frac{\Delta_{\text{opt}}}{|E_{\text{opt}}|}$ 
 $\delta_{\text{trunc}} = \frac{\Delta_{\text{trunc}}}{|E_{\text{opt}}|}$ 
if ( $|\delta_{\text{opt}}| < 10^{-14}$  or  $|\delta_{\text{trunc}}| < 10^{-14}$ ) then
     $\eta = 1$ 
else if  $\delta_{\text{trunc}} < 0$  then
     $\eta = 2(1 + \frac{|\delta_{\text{trunc}}|}{|\delta_{\text{opt}}|})$ 
else if  $\frac{|\delta_{\text{trunc}}|}{|\delta_{\text{opt}}|} < 0.05$  then
     $\eta = 1.2 - \frac{|\delta_{\text{trunc}}|}{|\delta_{\text{opt}}|}$ 
else if  $\frac{|\delta_{\text{trunc}}|}{|\delta_{\text{opt}}|} > 0.3$  then
     $\eta = \frac{1}{1.01}$ 
else
     $\eta = 1$ 
end if

```

Further, the adaption factor is restricted to $0.99 \leq \eta \leq 1.01$ and the mixing factor to $10^{-8} \leq \alpha \leq 100$. If the mixing factor falls below 10^{-8} , the subspace expansion is suspended entirely.

To achieve convergence of our DMRG3S+LBO method, it turns out to be beneficial to postpone the adaptation of the mixing factor α in the first few sweeps to keep it at a relatively high value. Furthermore, we noticed that the algorithm is still prone to getting stuck despite the use of the subspace expansion. This behavior is especially common in the CDW phase of the Holstein model when polarons become heavy and

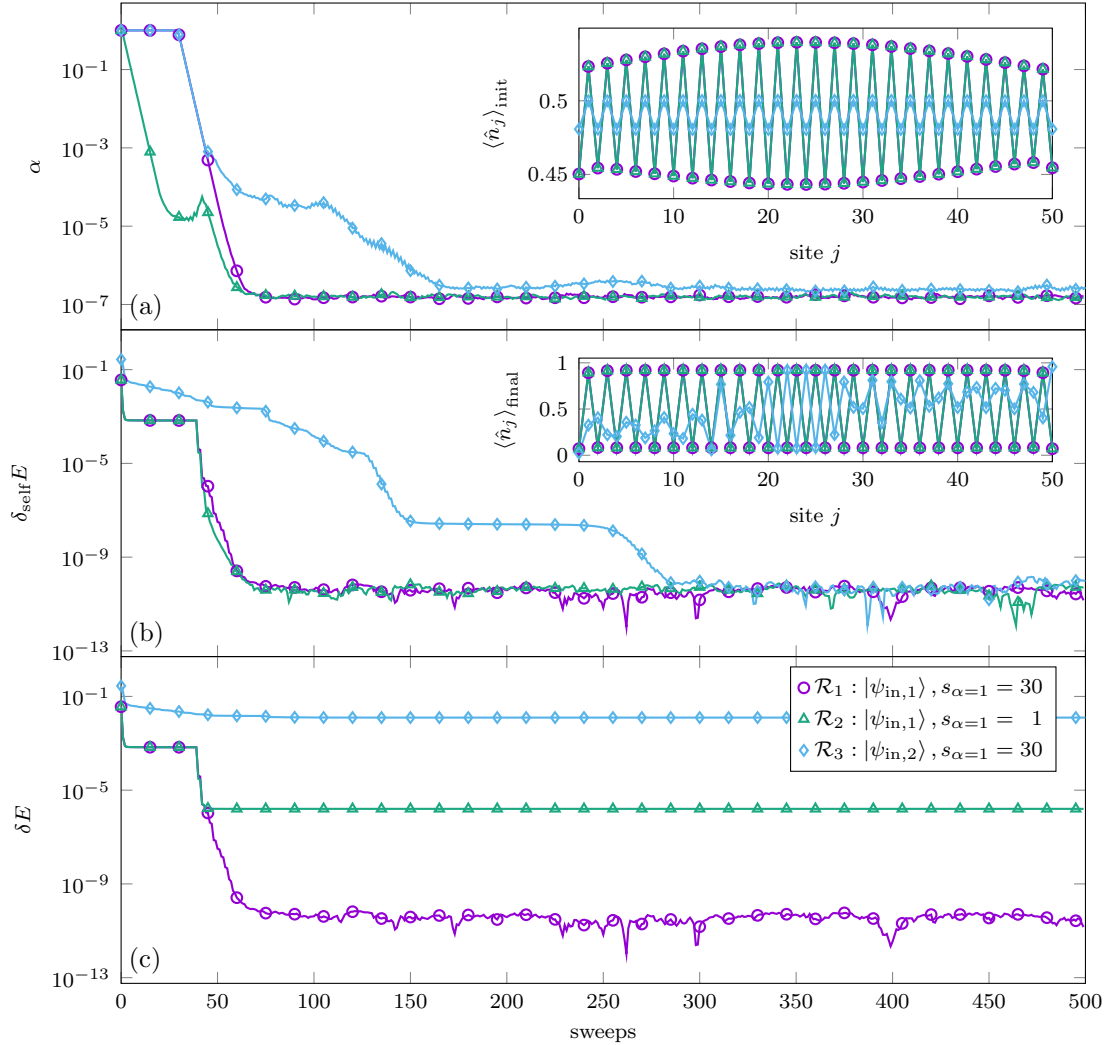


Figure 6. (a) Evolution of the subspace-expansion mixing factor during the sweeping. (b) Evolution of the relative energy distance during the sweeping to the best energy estimate in the runs. (c) Evolution of the relative energy distance during the sweeping to the best energy estimate in the run with the initial state $|\psi_{\text{in},1}\rangle$ and $s_{\alpha}=1=30$. Inset of (a): Electron density in the initial states. Inset of (b): Electron density in the final state. The system parameters are $L=51$, $N=25$, $\omega_0/t_0=1$, and $\gamma/t_0=2$. In all runs, $\chi=20$, $M_{\text{ph}}=31$, and $d_0=5$.

hard to move around in the lattice. It is therefore beneficial to use initial states that are already close to the targeted ground state and possess key features of it. We therefore pursue the strategy of first calculating the ground state at $\gamma=0$ for a relatively small maximal bond dimension, in an initialization run. In the following, we increase the coupling γ from run to run while keeping the maximal bond dimension fixed, until the desired coupling strength is reached. Then, the bond dimension is increased from run to run until the desired precision is reached.

We illustrate potential pitfalls of our method in figure 6. In this example, three runs with $L=51$, $\omega_0/t_0=1$, and $\gamma/t_0=2$, which corresponds to the CDW phase, are compared.

The maximal bond dimension is set to $m_{\max} = 20$, the maximum phonon number per site to $n_{\text{ph}} = 31$, and $d_o = 5$ optimal modes per symmetry block are considered. In the first run \mathcal{R}_1 , the initial state is the ground state at $\omega_0/t_0 = 1$, $\gamma/t_0 = 1.5$, $m_{\max} = 20$, $n_{\text{ph}} = 31$, and $d_o = 5$ ($|\Psi_{\text{in},1}\rangle$). Furthermore, the mixing factor α is fixed to 1 in the first 30 sweeps ($s_{\alpha=1} = 30$). In the second run \mathcal{R}_2 , the initial state is the same as in the first run ($|\Psi_{\text{in},1}\rangle$), but the fixation of α is only done in the first sweep ($s_{\alpha=1} = 1$). For the third run \mathcal{R}_3 , the initial state is chosen to be the ground state at $\gamma = 0$ and $m_{\max} = 15$ ($|\Psi_{\text{in},2}\rangle$), while α is again fixed for the first 30 sweeps ($s_{\alpha=1} = 30$).

The inset of figure 6(a) shows the electron density on the sites in the different initial states. As expected, the density profile is flatter in the ground state at $\gamma = 0$ ($|\Psi_{\text{in},2}\rangle$) and has more structure in the ground state at $\gamma/t_0 = 1.5$ ($|\Psi_{\text{in},1}\rangle$). In the main panel of figure 6(a), the mixing factor α is plotted against the sweeps. After the first 30 sweeps where α is fixed, the mixing factor falls off quickly to $\approx 10^{-7}$ in \mathcal{R}_1 . In \mathcal{R}_2 , the mixing factor falls off immediately with a small peak at around the 40th sweep before α also settles at $\approx 10^{-7}$. In \mathcal{R}_3 , the decay of α is more gradual but after the 160th sweep, it also has a value of $\approx 10^{-7}$ with small fluctuations.

In figure 6(b), the relative energy difference between the lowest energy found during the run and the current energy estimate in the middle of a specific sweep is presented:

$$\delta_{\text{self}}E = \frac{E_{\text{sweep}} - E_{\min,\text{run}}}{|E_{\min,\text{run}}|}. \quad (17)$$

The evolution of $\delta_{\text{self}}E$ can be extracted from a single run. In contrast, figure 6(c) displays the energy difference between the current energy estimate in the middle of a sweep and the lowest energy between all three runs:

$$\delta E = \frac{E_{\text{sweep}} - E_{\min}}{|E_{\min}|}. \quad (18)$$

It can, of course, only be extracted from a comparison between different runs.

The runs \mathcal{R}_1 and \mathcal{R}_2 show a plateau in $\delta_{\text{self}}E$ in figure 6(b) until approximately the 40th sweep. Then, the energy quickly drops over the course of about 20 sweeps and $\delta_{\text{self}}E$ stays below 10^{-10} after the 60th sweep. In contrast, the energy drops slower in \mathcal{R}_3 , but after the 300th sweep, $\delta_{\text{self}}E$ also stays below 10^{-10} .

While figure 6(b) suggests that all three runs are converged, the data for δE in figure 6(c) gives evidence that this is not the case. The data for \mathcal{R}_1 is the same in figure 6(b) and figure 6(c) since in \mathcal{R}_1 the lowest energy was found. \mathcal{R}_2 finds an energy that is about $\delta E \approx 10^{-6}$ above the one found by \mathcal{R}_1 . The energy found in \mathcal{R}_3 is $\delta E \approx 10^{-2}$ above the one of \mathcal{R}_1 .

The inset of figure 6(b) shows the real-space electron-density profile in the final states of the runs. The final states of \mathcal{R}_1 and \mathcal{R}_2 have the expected profile of a charge-density wave. The final state of \mathcal{R}_3 does not have such a structure in the electron density at all.

This example illustrates the impact of initial states and the choice of the mixing factor on the convergence of the DMRG3S+LBO. Choosing an initial state that already

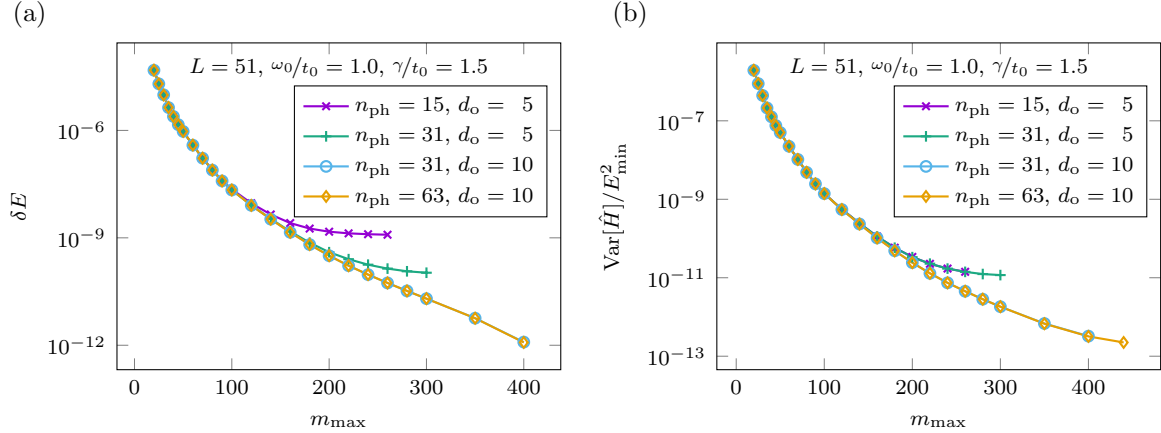


Figure 7. (a) Relative deviation of the ground-state energy obtained with DMRG3S+LBO from the smallest energy found, plotted against the maximal bond dimension m_{\max} . (b) Variance of the energy plotted against the maximal bond dimension m_{\max} .

possesses structural features of the ground state one is trying to find can prevent the algorithm from getting stuck in local minima. This can be achieved by gradually changing the parameters in the Hamiltonian (here γ) by performing several runs of complete ground-state searches. In this procedure, the initial state of the subsequent run is chosen to be the optimized ground state of the previous parameter set. Finally, the mixing factor should be fixed at a large value for the first few runs to explore a large enough portion of the Hilbert space before it can be lowered to achieve convergence.

2.3.4. Impact of n_{ph} and d_o on the precision of the ground state in the DMRG3S+LBO method In the DMRG3S+LBO method, the maximal bond dimension m_{\max} , the maximal number of phonons per site n_{ph} , and the maximal number of optimal modes per block d_o determine the reachable precision of the ground states. All of these parameters have a different influence. The maximal number of phonons per site n_{ph} changes the dimension of the Hilbert space and, in principle, the nature of the whole system. The ultimate goal is to get results that do not change upon further increase of n_{ph} and are therefore indistinguishable from the case $n_{\text{ph}} = \infty$. For smaller n_{ph} , results can be converged to a certain precision with respect to m_{\max} and d_o , but an increase of n_{ph} will still improve the precision substantially with respect to the $n_{\text{ph}} = \infty$ limit.

In figure 7, we compare the precision of the ground-state energy for different choices of m_{\max} , n_{ph} , and d_o . The system parameters are $L = 51$, $N = 25$, $\omega_0/t_0 = 1$, and $\gamma/t_0 = 1.5$. Figure 7(a) shows the relative difference between the energies at the end of each run to the best energy found:

$$\delta E = \frac{E_0(m_{\max}, n_{\text{ph}}, d_o) - E_{\min}}{|E_{\min}|}. \quad (19)$$

As a function of m_{\max} , the energy decreases as expected. For a certain choice of n_{ph} and d_o , the energy can, however, only reach a certain precision that does not substantially improve as the bond dimension is increased further. With $n_{\text{ph}} = 31$ and $d_o = 10$, the maximal precision of our implementation of the DMRG3S+LBO method can be reached, which turns out to be a relative energy difference of about 10^{-12} . Further increasing n_{ph} does not improve the energies.

Figure 7(b) shows the variance of the energy

$$\text{Var}[\hat{H}] = \langle \psi(m_{\max}, n_{\text{ph}}, d_o) | (H - E_0(m_{\max}, n_{\text{ph}}, d_o))^2 | \psi(m_{\max}, n_{\text{ph}}, d_o) \rangle \quad (20)$$

versus the maximal bond dimension m_{\max} . The variance can be taken as a measure of proximity of a certain state to an eigenstate of the Hamiltonian. As expected, a small choice of d_o limits the reachable precision in the variance. However, limiting n_{ph} does not limit the precision in such a way. As mentioned earlier, changing n_{ph} alters the Hilbert space and the system altogether and, therefore, one can be close to the ground state in the case of a small n_{ph} , but the state is still substantially different from the ground state in the limit $n_{\text{ph}} = \infty$. This difference, however, does not manifest itself in the variance.

2.4. Projected Purification

In the following, we describe the projected-purification ansatz [53], which is based on a doubling of the Hilbert space and a subsequent projection into an invariant subspace. This scheme allows us to formulate operators and states that transform under a restored global $U(1)$ symmetry and to efficiently represent and truncate the local phononic degrees of freedom. A simple pictorial representation of the ansatz is sketched in figure 8(a). Every physical site with electron and phonon degrees of freedom is accompanied by a phonon bath site that acts as a reservoir. Creating or annihilating a phonon on the physical site means that it hops from or to the bath site. This way, an artificial $U(1)$ symmetry is generated, namely the combined number of phonons on the physical and bath site is conserved.

2.4.1. Projected Purified Operators Consider a Hilbert space $\mathcal{H} = \mathcal{H}_d^{\otimes L}$ with basis states labeled by the eigenvalues of the local density operators $\hat{n}_j = \text{diag}(0, 1, \dots, d-1)$. We define a doubling $\mathcal{H}_{PB} = \mathcal{H}_P \otimes \mathcal{H}_B$, introducing two copies $\mathcal{H}_{P/B}$ of the original Hilbert space \mathcal{H} as shown in figure 8(a) and refer to \mathcal{H}_P and \mathcal{H}_B as the physical and bath Hilbert space, respectively. Operators acting on (local) Hilbert spaces $\mathcal{H}_{P/B(d)}$ will be equipped with an additional label, for instance, $\hat{n}_{P/B;j}$ denotes the density operators acting on the local physical or bath degrees of freedom at site j . A projected purified operator $\hat{O}_{PP} : \mathcal{P} \rightarrow \mathcal{P}$ acts on a subspace $\mathcal{P} \subset \mathcal{H}_{PB}$ of the purified Hilbert space and satisfies the constraints

$$\left[\hat{O}_{PP}, \hat{n}_{P;j} + \hat{n}_{B;j} \right] = 0 \quad (21)$$

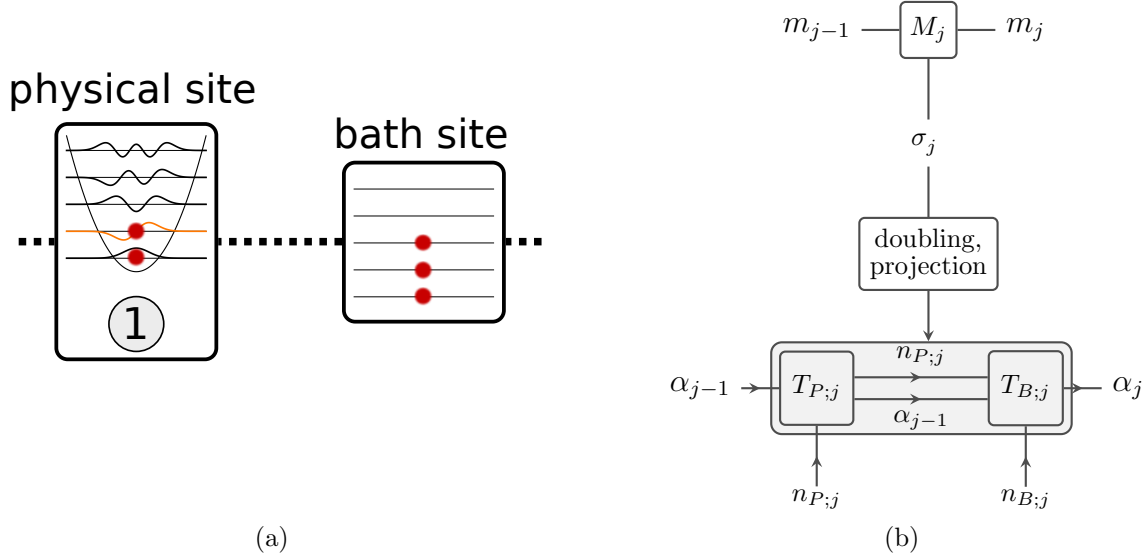


Figure 8. (a) A schematic representation of the local Hilbert space doubling via the introduction of a bath site for each local degree of freedom as used in PP-2DMRG is shown. (b) The decomposition and projection of a general MPS tensor (top) into the subspace \mathcal{P} enforcing the local gauge conditions is depicted. The decomposition of the introduced auxiliary index into irreducible representations of the local conservation law generated by $\hat{n}_{P;j} + \hat{n}_{B;j}$ as described in [53] is sketched by the double bond ($n_{P;j}, \alpha_{j-1}$).

for every j . Defining global operators $\hat{N}_{P/B} = \sum_j \hat{n}_{P/B;j}$, any projected purified operator manifestly conserves the global $U(1)$ symmetry generated by $\hat{N}_P + \hat{N}_B$:

$$[\hat{O}_{PP}, \hat{N}_P + \hat{N}_B] = 0. \quad (22)$$

An explicit construction scheme for the subspace \mathcal{P} can be found by fixing gauge constraints between the physical and bath site to

$$\hat{n}_{P;j} + \hat{n}_{B;j} \equiv (d-1). \quad (23)$$

In [53], we showed that this choice implies $\dim \mathcal{P} = \dim \mathcal{H}$ and that there is a one-to-one mapping between states and operators in these Hilbert spaces. It follows that for any operator \hat{O} acting on the original Hilbert space, an analogous projected purified operator can be constructed. This is achieved by introducing balancing operators $\hat{\beta}_{B;j}^{[\dagger]}$

$$\hat{\beta}_{B;j} = \sum_{n_{B;j}=1}^{d-1} |n_{B;j}-1\rangle \langle n_{B;j}|, \quad |n_{B;j}\rangle \in \mathcal{H}_{B;d}. \quad (24)$$

Writing \hat{O} in terms of ladder operators $\hat{b}_j^{[\dagger]}$, the mapping to the corresponding projected purified operator \hat{O}_{PP} is achieved by pairing up ladder operators with conjugated

balancing operators:

$$\hat{b}_j^\dagger \rightarrow \hat{b}_{P;j}^\dagger \hat{\beta}_{B;j}, \quad \hat{b}_j \rightarrow \hat{b}_{P;j} \hat{\beta}_{B;j}^\dagger. \quad (25)$$

The phononic part of the Holstein model breaking the global $U(1)$ symmetry in \mathcal{H} is then represented by a projected purified operator $\hat{H}_{PP;f-ph}$ acting only on \mathcal{P}

$$\hat{H}_{PP;f-ph} = \gamma \sum_j \hat{n}_j^f \left(\hat{b}_{P;j}^\dagger \hat{\beta}_{B;j} + \hat{b}_{P;j} \hat{\beta}_{B;j}^\dagger \right). \quad (26)$$

Note that $\hat{H}_{PP;f}$ and $\hat{H}_{PP;ph}$ remain unaltered except for a formal replacement of local operators acting on \mathcal{H}_d with their counterparts acting on \mathcal{P} :

$$\hat{c}_j^{[\dagger]} \rightarrow \hat{c}_{P;j}^{[\dagger]} \hat{\mathbf{1}}_{B;j}, \quad \hat{n}_j^f \rightarrow \hat{n}_{P;j}^f \hat{\mathbf{1}}_{B;j} \quad \text{and} \quad \hat{b}_j^\dagger \hat{b}_j \rightarrow \hat{b}_{P;j}^\dagger \hat{b}_{P;j} \hat{\mathbf{1}}_{B;j}. \quad (27)$$

2.4.2. Projected Purified MPS The gauge-fixing condition (23) allows us to construct a projector to \mathcal{P} . Using the action of this projector on MPSs in the enlarged Hilbert space, we derived a condition on the combined physical and bath system's site tensors [53]. In a practical ground-state-search calculation, it suffices to create an initial state whose physical indices reflect the gauge fixing. For instance, let $T_{j;\alpha_{j-1},\gamma_j}^{n_{P;j}}$ and $T_{j;\gamma_j,\alpha_j}^{n_{B;j}}$ be $U(1)$ -invariant MPS site tensors with physical and bath local degrees of freedom labeled by $n_{P;j}$ and $n_{B;j}$, respectively. The condition for the MPS to represent a projected purified state $|\psi\rangle_{PP} \in \mathcal{P}$ is then given by

$$\sum_{\gamma_j} T_{j;\alpha_{j-1},\gamma_j}^{n_{P;j}} T_{j;\gamma_j,\alpha_j}^{n_{B;j}} \neq 0 \Leftrightarrow n_{P;j} + n_{B;j} \equiv (d-1), \quad (28)$$

and shown graphically in figure 8(b). Since \mathcal{P} is a subspace of the enlarged Hilbert space \mathcal{H}_{PB} , projected purified operators acting on such states conserve this condition. This is an important point as it minimizes the implementational effort. In fact, by doubling the Hilbert space and using projected purified operator representations only, DMRG codes that are able to initialize states $|\psi\rangle_{PP}$ obeying (28) can readily work in \mathcal{P} and thereby exploit restored global $U(1)$ symmetries. For the dimensions of the indices representing the local degrees of freedom, this implies $\dim n_{P/B;j} \equiv 1$.

2.4.3. Truncation and Connection to Single-Site Reduced Density Matrix Projected purified states $|\psi\rangle_{PP} \in \mathcal{P}$ exhibit an intimate relation to the single-site reduced density matrix $\rho_{n_j, n'_j} = \text{Tr}_{k \neq j} |\psi\rangle \langle \psi|$ of the corresponding state in the original Hilbert space \mathcal{H} , which is displayed graphically in figure 9. The crucial observation is that in a mixed-canonical MPS representation, when tracing out the auxiliary indices of the physical Hilbert space \mathcal{H}_P at the orthogonality center j , one obtains the diagonal elements

$$\rho_{n_{P;j}, n_{P;j}} = \sum_{\alpha_{j-1}, \gamma_j} T_{j;\alpha_{j-1}, \gamma_j}^{n_{P;j}} \left[T_{j;\alpha_{j-1}, \gamma_j}^{n_{P;j}} \right]^\dagger, \quad (29)$$

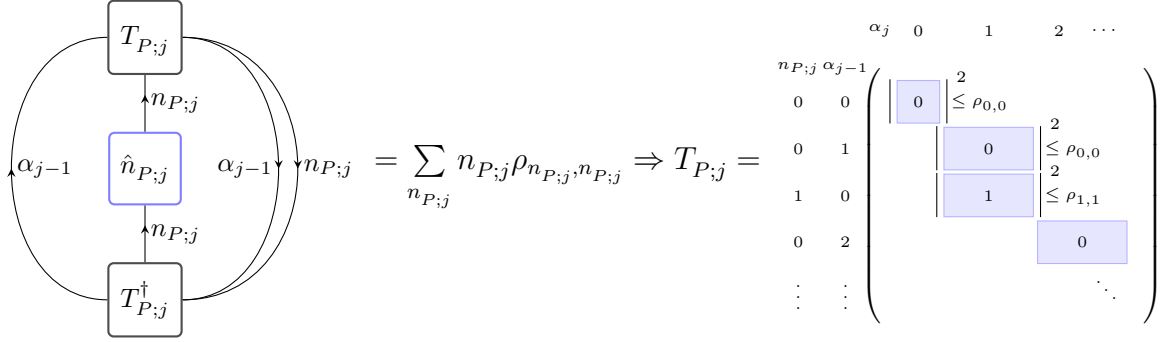


Figure 9. Schematic representation of the connection between the irreducible representations of tensor blocks $T^{n_{P;j}}$ and the diagonal elements of the single-site reduced density matrix $\rho_{n_{P;j}, n_{P;j}}$. On the right-hand side, the blue boxes indicate irreducible representations of the tensor blocks $T^{n_{P;j}}$ with $n_{P;j} = 0, 1, 2, \dots$ constituting the site tensor $T_{P;j}$. Note that if $\rho_{n_{P;j}, n_{P;j}}$ is smaller than the given truncation threshold, complete tensor blocks $T^{n_{P;j}}$ can be discarded.

of ρ_{n_j, n'_j} . A truncation scheme across the auxiliary bond γ_j :

$$T_{j; \alpha_{j-1}, \gamma_j}^{n_{P;j}} = \sum_{\sigma} U_{j; \alpha_{j-1}, \sigma}^{n_{P;j}} \Lambda_{\sigma} V_{\sigma, \gamma_j}, \quad (30)$$

discarding only the smallest singular values $\Lambda_{\tilde{\sigma}}$ so that the truncated weight fulfills $\sum_{\tilde{\sigma}} \Lambda_{\tilde{\sigma}}^2 < \delta$, approximates the single-site reduced density-matrix in an optimal way with respect to the 1-norm

$$\text{Tr}(\rho_{n_j, n'_j} - \tilde{\rho}_{n_j, n'_j}) < \delta. \quad (31)$$

Such a truncation can discard complete tensor blocks $T^{n_{P/B;j}}$ if $\rho_{n_{P;j}, n_{P;j}} < \delta$ as follows immediately from (29) and thus reduces the number of local degrees of freedom $n_{P/B;j}$ in the state representation.

Finally, the full single-site reduced density matrix can be obtained from contracting physical and bath site tensors in a mixed-canonical representation

$$M_{j; \alpha_{j-1}, \alpha_j}^{n_j} = \sum_{\gamma_j} T_{j; \alpha_{j-1}, \gamma_j}^{n_{P;j}} T_{j; \gamma_j, \alpha_j}^{n_{B;j}} \delta_{n_j, n_{P;j}} \quad (32)$$

$$\Rightarrow \rho_{n_j, n'_j} = \sum_{\alpha_{j-1}, \alpha_j} M_{j; \alpha_{j-1}, \alpha_j}^{n_j} \left[M_{j; \alpha_{j-1}, \alpha_j}^{n'_j} \right]^\dagger. \quad (33)$$

Taking operators and states into their projected purified representation implies certain numerical advantages in MPS calculations when the local dimension d of the problem is large and the system does not conserve global $U(1)$ symmetries, initially. When re-establishing a global $U(1)$ -symmetry in the subspace \mathcal{P} , local degrees of freedom $\hat{n}_{P/B;j}$ decompose into one-dimensional representations. As a consequence, contractions scaling as d^l for some exponent $l \in \mathbb{N}$ can be parallelized over the local degrees of freedom.

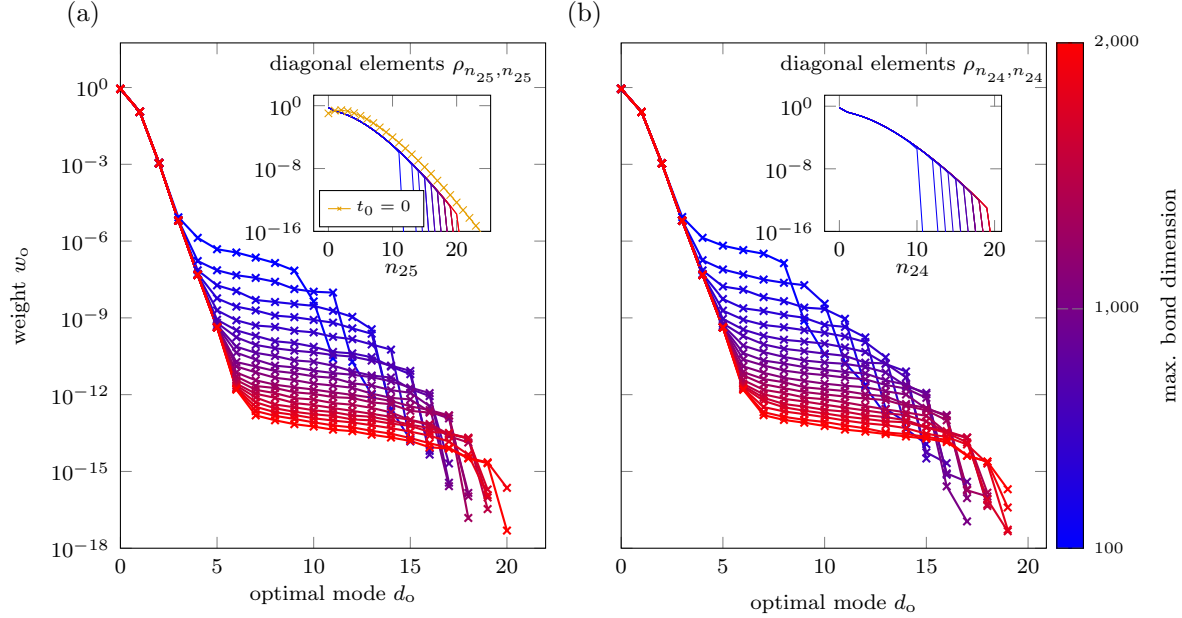


Figure 10. Weight w_o of optimal modes d_o as a function of the maximal bond dimension at the auxiliary bonds γ_{25} (a) and (b) using the projected purification. Data is extracted from the single-site reduced density matrix $\rho_{n_{25/24}, n'_{25/24}}$ at the center site ($j = 25/24$) in the calculated ground state of the Holstein model with $L = 51$ sites and $N = 25$ fermions, $\omega/t_0 = 1.0$, $\gamma/t_0 = 1.5$. The inset shows the diagonal elements $\rho_{n_{25}, n_{25}}$ indicating the immediate effect of truncations. For comparison, the phonon excitation probabilities obtained for $t_0 = 0$ at occupied sites (left) are overlayed, indicated by yellow crosses.

Additionally, the connection to the single-site reduced density matrix reveals that if for some $n_0 \in \{0, \dots, d-1\}$ the diagonal elements $\rho_{n \pm n_0, n \pm n_0}$ are decaying fast enough, the number of relevant tensor blocks can be reduced drastically upon truncation. An important conclusion is that having restored the global $U(1)$ symmetry w.r.t. phononic degrees of freedom allows us to employ a local solver based on two-site tensors, which is less prone of getting stuck in local minima (PP-2DMRG). Furthermore, the truncation argument implies that the dimension of the auxiliary bond γ_j between physical and bath site tensors controls the quality of the approximation of ρ_{n_j, n'_j} .

As a consequence, the same scaling analysis in terms of auxiliary bond dimensions, which is usually employed in DMRG algorithms to extrapolate observables towards their exact value, can be used for the projected purification. This is demonstrated in figure 10(a), where we show the weight w_o of the optimal modes d_o of the single-site reduced density-matrix as a function of the auxiliary bond dimension γ_j used to approximate the ground state of the Holstein model near the phase boundary (P.2). Upon increasing the bond dimension we find a well-converging behavior for the weights $w_o(d_o)$. Note that in these calculations, we allowed for a maximum number of $n_{\text{ph}} = 63$ phonons per lattice site. However, as shown in the inset, the maximum occupation

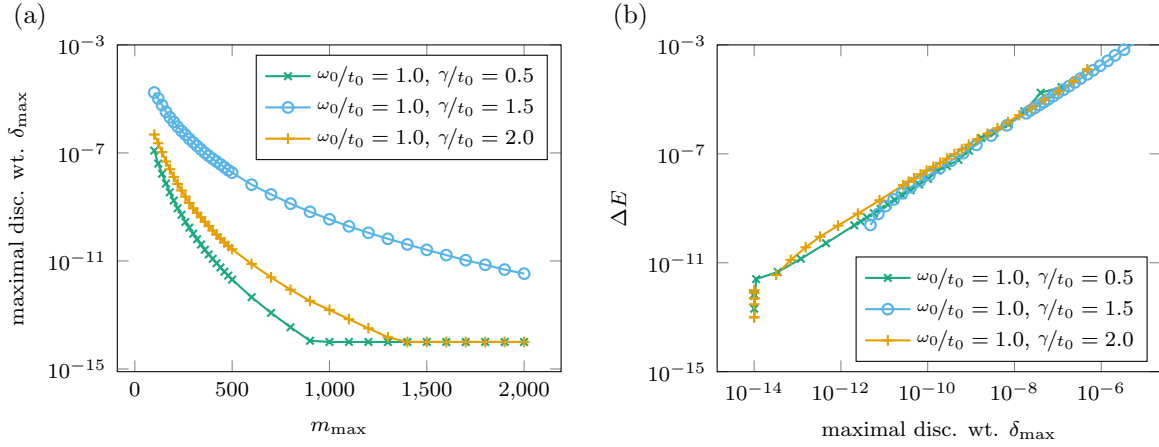


Figure 11. Truncation effects in the PP-2DMRG method at three different points in parameter space, i.e., in the LL phase (P.3) (green), near the phase boundary (P.2) (blue), and in the CDW phase (P.3) (yellow). In (a), the maximal discarded weight δ_{\max} as a function of the maximally allowed bond dimension m_{\max} is shown demonstrating the impact of strong fluctuations near the phase boundary on the required bond dimensions to achieve a particular accuracy. (b) shows the scaling of the relative distance ΔE to the minimally found ground-state energies with the maximal discarded weight revealing that near the phase boundary, the maximally allowed number of states $m_{\max} = 2000$ is not sufficient to achieve the same numerical precision as in the LL and CDW phase.

number for the phonons kept after truncation is $n_{\text{ph}} \leq 20$, i.e., a significant amount of tensor blocks is discarded due to the vanishing contribution of high-occupation phonon modes. Therein, we also indicate the diagonal elements calculated for the atomic limit $t_0 = 0$ using the Lang-Firsov transformation of the Holstein Hamiltonian [79]. It can be seen that the phonon excitation probability (i.e., ρ_{n_j, n_j}), obtained from projected purification, is already very close to the limit of decoupled fermions, which is the asymptotic distribution when sending $t_0 \rightarrow 0$.

2.4.4. Effects of Truncation Performing ground-state searches using PP-2DMRG allows to monitor the actual discarded weight $\delta_{\bar{j}}$ on a bond $\bar{j} = (j, j + 1)$ after each, local-optimization step as a function of the maximally allowed bond dimension m_{\max} . As a consequence, an estimate for the quality of the obtained ground-state energy can be constructed from the maximally found discarded weight per bond

$$\Delta = 2L \max_{\bar{j}} \delta_{\bar{j}} \equiv 2L\delta_{\max}. \quad (34)$$

This provides an alternative convergence test for the approximation of the ground state as we expect the difference of the approximated energy E to the exact ground-state energy E_{ex} to scale as $\frac{E - E_{\text{ex}}}{E_{\text{ex}}} \sim \Delta$. For PP-2DMRG, this is important, since the phonon correlations are encoded into the auxiliary bond between the physical- and bath-site

tensors. If the number of phonons is large and their excitation probability is broadly distributed, this implies the requirement of significantly larger auxiliary bond dimensions to keep the discarded weight below a certain threshold [53].

The necessity to monitor the discarded weight can be illustrated by studying the system near the phase boundary where strong fluctuations in both the fermionic and phononic subsystem are present, which have to be captured by the auxiliary bonds. The bond dimensions between the original lattice sites are multiplied by the additional number of states required to capture the phononic degrees of freedom on the auxiliary bonds γ_j . Thus, near the phase boundary, where we have strong fluctuations on large length scales also in the fermionic systems, the value of m_{\max} on the auxiliary bonds between physical and bath sites has to be chosen comparably large in order to achieve a certain quality Δ of the approximated ground states. We demonstrate this observation in figure 11(a) (blue curve) where the chosen cutoff $m_{\max} = 2000$ is not sufficient to reach the desired discarded weight per bond $\delta_j = 10^{-14}$. However, it should be pointed out that using the restored global $U(1)$ symmetries, $m_{\max} = 2000$ is not fixed because of numerical limitations, but only to allow consistent comparisons.

2.4.5. Benchmark Setup For the benchmark simulations, the maximum allowed bond dimensions are varied from $m_{\max} = 100$ up to $m_{\max} = 2000$ and the number of phonons is bound by $n_{\text{ph}} = 63$. The initial state for the ground-state searches are constructed as a Fermi sea of non-interacting, spinless fermions and no phonons in the physical system ($n_{P;j} \equiv 0$). In order to achieve convergence, the maximally allowed number of sweeps for a single ground-state calculation was set to 200 (which is never reached) and the calculations were terminated once the relative fluctuations in the approximated ground-state energy as a function of the number of sweeps fell below a certain threshold. For the high-precision calculations, this threshold was set to 10^{-14} while in case of the finite-size extrapolation the condition to terminate the ground-state search was relaxed to a threshold of 10^{-8} .

3. Comparing the Methods

The Holstein model provides an excellent testing platform to compare the numerical behavior of the presented DMRG methods with respect to two important problem settings: numerical high-precision calculations at intermediate system sizes and finite-size extrapolations, thereby relaxing conditions on the numerical precision as a tradeoff for reaching larger system sizes. For the high-precision calculations, we fix the system size to $L = 51$ lattice sites at nearly half filling with $N = 25$ fermions. The finite-size extrapolation is performed for systems with $L = 51, 101, 151, 201$ lattice sites where the fermion number is set to $N = \frac{L-1}{2}$. Note that we always use an odd number of lattice sites. One reason for this is the observation that in the CDW phase, the sublattice symmetry between even and odd sites is broken and the unit cell is enlarged to consist of two lattice sites. In a system with an even L , this yields two different possibilities

of arranging the unit cells. These two choices will hybridize to form the ground state. For DMRG, this is a delicate situation as the site tensors are optimized in a way to minimize entanglement entropy while sweeping through the system. In such situations, an often encountered consequence is that algorithms get stuck in low-lying excited states, which minimize the entanglement entropy but not the global energy. To circumvent this problem, we use odd system sizes, thereby fixing the arrangement of the unit cells in the CDW phase. This has the pleasant side effect that the CDW order parameter actually acquires a finite value in the CDW phase, which is not the case in finite systems with an even number of sites.

3.1. Convergence Analysis of Ground-State Energies

In order to compare the methods' capabilities of approximating the ground state, we perform a scaling analysis in the maximum bond dimension m_{\max} . We calculate the relative distance of the approximated ground-state energies $E_0(m_{\max}) = \langle \psi(m_{\max}) | \hat{H} | \psi(m_{\max}) \rangle$ to the lowest energy found from all methods, E_{\min} ,

$$\Delta E(m_{\max}) = \frac{E_{\min} - E_0(m_{\max})}{E_{\min}}. \quad (35)$$

For the DMRG3S+LBO and PP-2DMRG methods, we also systematically evaluated the variance for the found ground-state approximations $|\psi(m_{\max})\rangle$

$$\text{Var}[\hat{H}] = \langle \psi(m_{\max}) | (\hat{H} - E_0(m_{\max}))^2 | \psi(m_{\max}) \rangle. \quad (36)$$

In practice, a systematic dependency of the variance on the ground-state energy allows us to extrapolate toward the limit of infinite bond dimension $E_0(m_{\max} \rightarrow \infty)$ [80].

During the numerical calculations, the maximally allowed discarded weight per bond is set to $\delta = 10^{-14}$ for the DMRG3S+LBO and PP-2DMRG methods. The PS-DMRG calculations were not limited with respect to δ . Here, for the given parameter sets, the discarded weight is not a helpful quantity to decide whether a calculation converges or not and therefore, for PS-DMRG, we focus on the bond dimension as the sole control parameter.

Having discussed each method's peculiarities in sections 2.2 to 2.4, in the following, we only show one dataset per method and parameter set. For the comparison, we pick those datasets yielding the lowest ground-state energies for the largest bond dimension.

LL phase Figure 12 displays the results of the scaling analysis in the LL phase (P.1). The maximum bond dimension m_{\max} used during the PS-DMRG and PP-2DMRG calculations are rescaled by a factor of 3. For the latter, this yields a dependency of the ground-state energies on m_{\max} comparable to the data obtained using DMRG3S+LBO, as shown in figure 12(a). The smallest ground-state energy reached is $E_{\min}/t_0 = -36.15999956298296$ obtained by PP-2DMRG with a relative precision $\sim 10^{-13}$, which is consistent with the chosen discarded weight $\delta = 10^{-14}$.

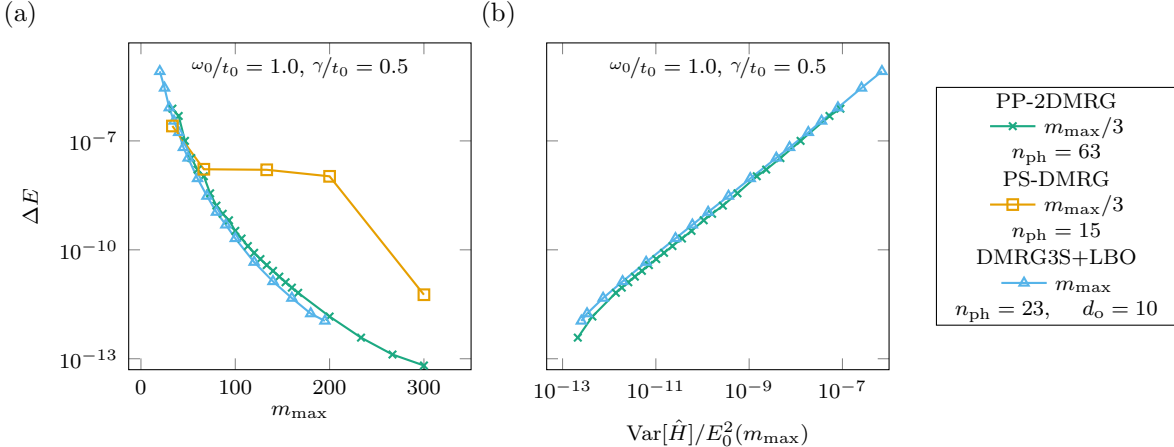


Figure 12. Relative deviations from the minimal ground-state energy found (a) and their scaling w.r.t. the relative variance (b) using PS-DMRG (ΔE only), PP-2DMRG and DMRG3S+LBO for the parameter set (P.1). We vary the maximal bond dimensions and for the case of PS-DMRG and DMRG3S+LBO, we only show data points belonging to those datasets that yield the lowest ground-state energies. The maximal bond dimensions m_{\max} in (a) are rescaled by a factor of 3 in the case of the PS-DMRG and PP-2DMRG calculations.

The relative variance $\frac{\text{Var}[\hat{H}]}{E_0^2(m_{\max})}$ as a function of the relative distance ΔE is shown in figure 12(b). For both the DMRG3S+LBO and PP-2DMRG methods, we find a similar systematic dependence up to a very high precision. Note that the saturation of $\frac{\text{Var}[\hat{H}]}{E_0^2(m_{\max})}$ at $\Delta E(m_{\max}) < 10^{-12}$ is numerically consistent with the overall truncation error $\propto L \cdot \delta$ introduced by the chosen discarded weight per bond $\delta = 10^{-14}$.

Phase boundary Figure 13 shows the results near the phase boundary between the LL and CDW phase. The scaling of $\Delta E(m_{\max})$ displayed in figure 13(a) reveals that the appearance of heavy polarons and strong fluctuations in the fermion system require a much larger bond dimension to approximate the ground state with a high precision. This is reflected by a rescaling of m_{\max} with a factor of 1.5 for the PS-DMRG method and a factor of 5 for PP-2DMRG in order to achieve a convergence behavior similar to the one observed in DMRG3S+LBO. Here, the ground-state approximations obtained using DMRG3S+LBO yield the smallest energy, which is given by $E_{\min}/t_0 = -70.862628874727$ with a relative precision of $\lesssim 10^{-11}$ as can be seen by the variance displayed in figure 13(b).

CDW phase In figure 14, the scaling analysis is shown for the parameter set (P.3) for which the system is in the CDW phase. All tested methods are capable of faithfully representing the ground state with a very high precision and comparably small bond dimensions with the lowest energy given by $E_{\min}/t_0 = -107.32209423031215$ with a relative precision of 10^{-14} using PP-2DMRG. For the PS-DMRG method, we rescaled

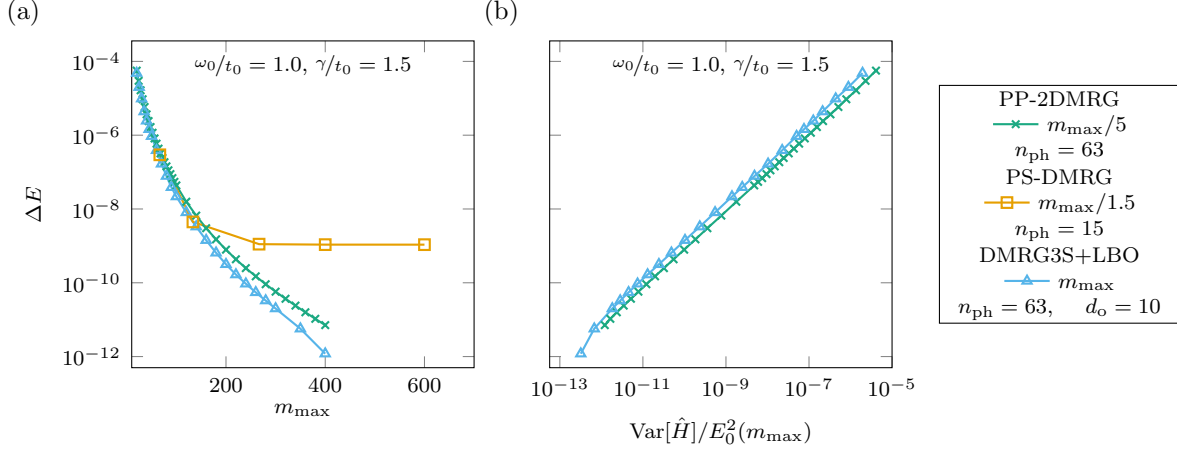


Figure 13. Relative deviations from the minimal ground-state energy found (a) and their scaling w.r.t. the relative variance (b) using PS-DMRG (ΔE only), PP-2DMRG and DMRG3S+LBO for the parameter set (P.2). We vary the maximal bond dimensions and for the case of PS-DMRG and DMRG3S+LBO, we only show data points belonging to those datasets that yield the lowest ground-state energies. The maximal bond dimensions m_{\max} in (a) are rescaled by a factor of 1.5 in the case of the PS-DMRG calculations and a factor of 5 in the case of the PP-2DMRG calculations.

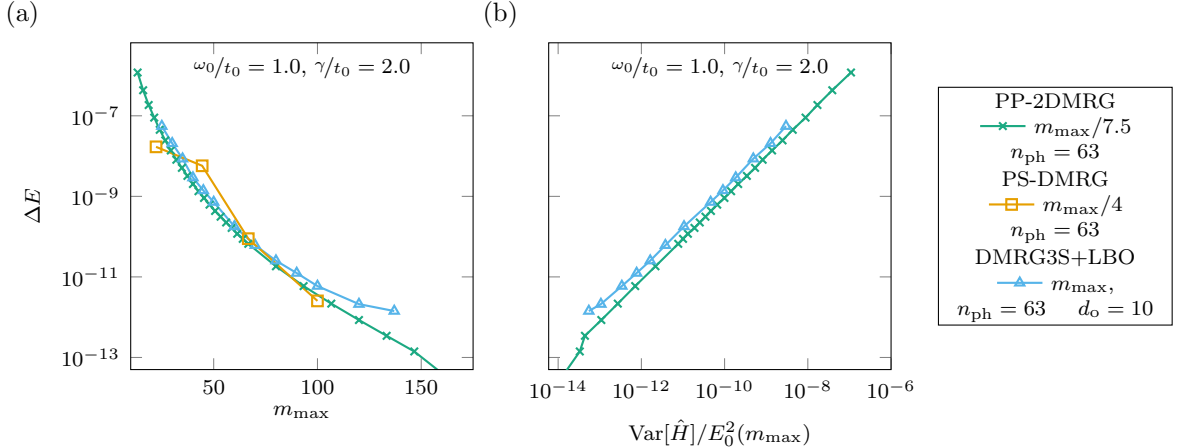


Figure 14. Relative deviations from the minimal ground-state energy found (a) and their scaling w.r.t. the relative variance (b) using PS-DMRG (ΔE only), PP-2DMRG and DMRG3S+LBO for the parameter set (P.3). We vary the maximal bond dimensions and for the case of PS-DMRG and DMRG3S+LBO, we only show data points belonging to those datasets that yield the lowest ground-state energies. The maximal bond dimensions m_{\max} in (a) are rescaled by a factor of 4 in the case of the PS-DMRG calculations and a factor of 7.5 in the case of the PP-2DMRG calculations.

the maximally allowed bond dimension by a factor of 4 while a factor of 7.5 was required for the PP-2DMRG method in order to achieve a similar scaling behavior of ΔE for the three methods. This large rescaling factor is based on the broadly distributed excitation

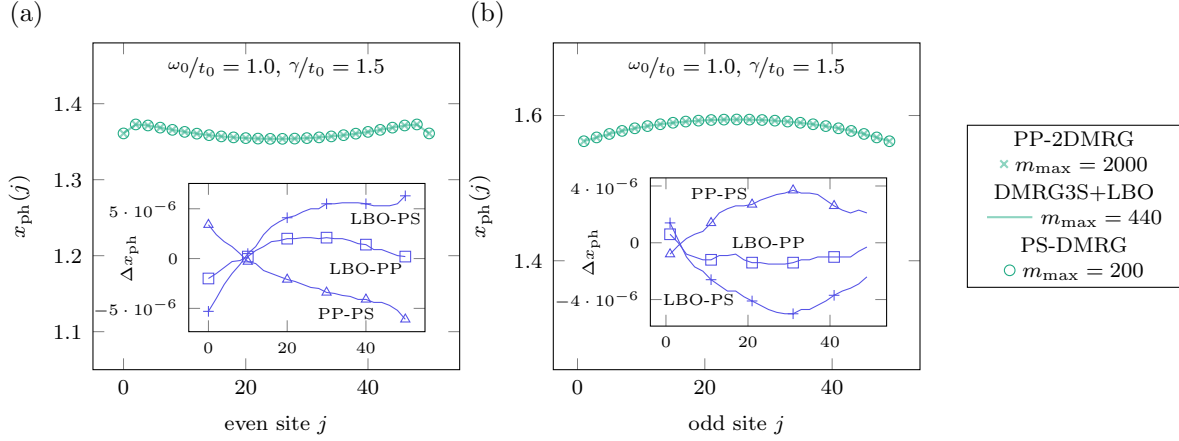


Figure 15. Oscillator displacement $x_{\text{ph}}(j) = \langle \hat{b}_j^\dagger + \hat{b}_j \rangle$ in the ground state near the phase boundary. The data shown here is taken from the calculations with the largest bond dimension for each method. For convenience, even-(a) and odd-site (b) expectation values are plotted separately. Insets display differences of the calculated oscillator displacements between the different methods.

probabilities of the phonons requiring a larger local Hilbert-space dimension. Here, for all three methods tested, we use $N_{\text{ph}} = 63$ to achieve the best results.

3.2. Local Observables - Oscillator Displacement

Having studied the convergence of the ground-state approximation for the different methods, we turn to physical observables next. In the Holstein model, the CDW phase is characterized by the formation of lattice distortions with a period of twice the lattice constant, i.e., the translation symmetry of the lattice is broken into two translational invariant sublattices \mathcal{A}/\mathcal{B} with even/odd lattice sites. We evaluate the oscillator displacement of the j th lattice site for different maximum bond dimensions m_{max} near the phase boundary (P.2)

$$x_{\text{ph}}(j) = \langle \hat{b}_j^\dagger + \hat{b}_j \rangle , \quad (37)$$

breaking translational symmetry. In figure 15, the results are shown for $\omega_0/t_0 = 1.0$ and $\gamma/t_0 = 1.5$. We separately plot even-(figure 15(a)) and odd-site (figure 15(b)) expectation values to illustrate the behavior of $x_{\text{ph}}(j)$ in the two sublattices. All methods yield the same behavior, i.e., we find developing CDW modulations in the two sublattices caused by finite displacements with larger values $x_{\text{ph}}(j)$ for $j \in \mathcal{B}$ compared to those $x_{\text{ph}}(j)$ for $j \in \mathcal{A}$. In order to visualize the numerical deviations, in the insets, we plot the difference $\Delta x_{\text{ph}}(j)$ between the displacements obtained from the datasets with the largest m_{max} for each method, as they exhibit the highest precision ($m_{\text{max}} = 2000$ for PP-2DMRG, $m_{\text{max}} = 440$ for DMRG3S+LBO and $m_{\text{max}} = 200$ for PS-DMRG). In the analyzed data, the deviations $\Delta x_{\text{ph}}(j)$ rapidly decrease and, for the largest bond dimensions, are located around 10^{-6} as shown in figure 15.

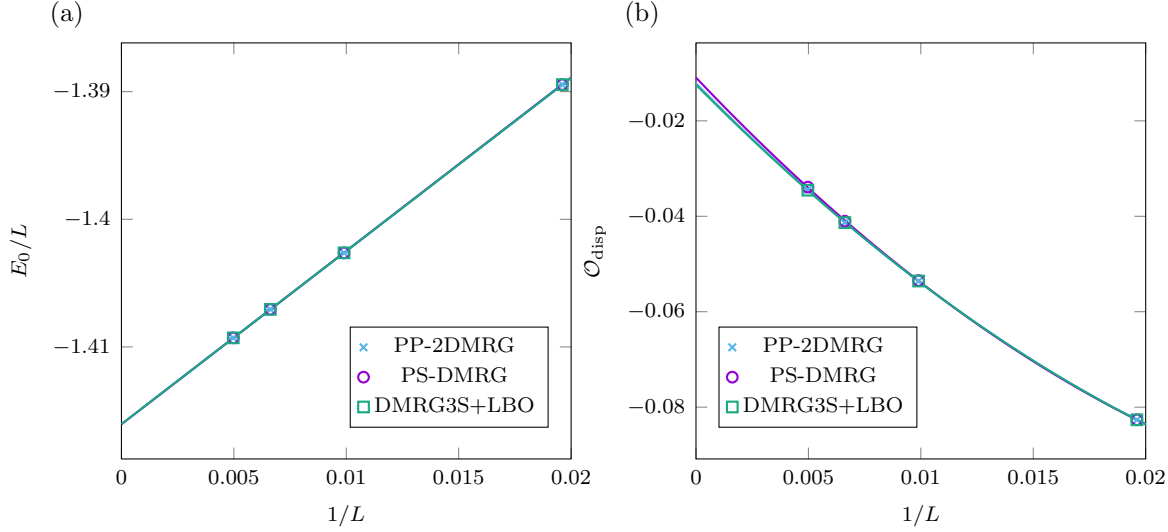


Figure 16. (a) Finite-size scaling of the ground-state energy of the Holstein model. (b) Finite-size scaling for the CDW order parameter of the Holstein model. The model is evaluated for parameters $\omega_0/t_0 = 1.0$, $\gamma/t_0 = 1.5$ at nearly half filling where we set $N = \frac{L-1}{2}$.

3.3. Finite-Size Extrapolation

Practically, one is often interested in a finite-size extrapolation of intensive quantities such as the energy density $\frac{E_0}{L}$ or the order parameter

$$\mathcal{O}_{\text{disp}}(L) = \frac{1}{L} \sum_j (-1)^j x_{\text{ph}}(j) , \quad (38)$$

where the extrapolation towards $L \rightarrow \infty$ allows us to approach the thermodynamic limit. Here, we perform a scaling analysis of the ground-state energy density $\epsilon(L) = \frac{E_0}{L}$ in units of $t_0 \equiv 1$ and $\mathcal{O}_{\text{disp}}(L)$. The extrapolations are done using fitting functions

$$\epsilon(L) = \frac{A_\epsilon}{L} + \epsilon_\infty \quad (39)$$

$$\mathcal{O}_{\text{disp}}(L) = \frac{A_{\mathcal{O}}}{L} + \frac{B_{\mathcal{O}}}{L^2} + \mathcal{O}_{\text{disp},\infty} . \quad (40)$$

For the order parameter, we add a contribution $\propto \frac{1}{L^2}$ to account for boundary effects, which are important for the parameter sets (P.1) and (P.2).

Energy density The extrapolated energy density in the thermodynamic limit is shown in table 1. All methods agree within their confidence intervals for the investigated parameter sets (P.1) and (P.2). For illustrational purposes, in figure 16(a), the finite-size extrapolation is displayed for the parameter set (P.2). In the CDW phase (P.3), the finite-size extrapolations seem to underestimate the fitting error. We attribute

Table 1. Energy densities $\varepsilon_\infty = \lim_{L \rightarrow \infty} \varepsilon(L)$ in units of t_0 obtained from finite-size scaling of ground-state energies.

	PS-DMRG	DMRG3S+LBO	PP-2DMRG
(P.1)	$-0.71862 \pm (2 \cdot 10^{-5})$	$-0.718616 \pm (5 \cdot 10^{-6})$	$-0.71863 \pm (1 \cdot 10^{-5})$
(P.2)	$-1.41606 \pm (1 \cdot 10^{-5})$	$-1.416048 \pm (7 \cdot 10^{-6})$	$-1.416052 \pm (6 \cdot 10^{-6})$
(P.3)	$-2.1462830 \pm (1 \cdot 10^{-7})$	$-2.146283452 \pm (2 \cdot 10^{-9})$	$-2.146283443 \pm (2 \cdot 10^{-9})$

Table 2. Order parameters $\mathcal{O}_{\text{disp},\infty} = \lim_{L \rightarrow \infty} \mathcal{O}_{\text{disp}}(L)$ obtained from the finite-size scaling of ground-state values.

	PS-DMRG	DMRG3S+LBO	PP-2DMRG
(P.1)	$(-2.2 \pm 0.4) \cdot 10^{-5}$	$(-3 \pm 6) \cdot 10^{-6}$	$(-5.3 \pm 0.9) \cdot 10^{-6}$
(P.2)	$(-1.09 \pm 0.06) \cdot 10^{-2}$	$(-1.24 \pm 0.03) \cdot 10^{-2}$	$(-1.21 \pm 0.04) \cdot 10^{-2}$
(P.3)	$-1.678313 \pm (5 \cdot 10^{-6})$	$-1.678221 \pm (4 \cdot 10^{-6})$	$-1.678244 \pm (5 \cdot 10^{-6})$

this to the fact that in the CDW phase, and at weakened conditions on the precision, the formation of heavy polarons effectively suppresses the energy gains due to fermion delocalization. As a consequence, domain walls in the fermionic system are harder to resolve and the calculations can get stuck in a local minimum. In our calculations, it appears that all three methods are affected by this problem, though in a different way owing to their different approximations, and practically, convergence has to be checked very carefully.

Order parameter The extrapolated values for the CDW order-parameter in the thermodynamic limit are shown in table 2; and the explicitly calculated system-size dependencies are plotted in figure 16(b) for the parameter set (P.2). In the LL phase (P.1), we expect $\mathcal{O}_{\text{disp},\infty} \equiv 0$. With a relative precision $\sim \mathcal{O}(10^{-5})$, this is found for the PS-DMRG method, whereas the PP-2DMRG and DMRG3S+LBO calculations are about an order of magnitude smaller $\sim \mathcal{O}(10^{-6})$. Near the phase boundary (P.2), all methods yield a small but finite value coinciding with a relative precision of $\sim \mathcal{O}(10^{-2})$, which is comparably small and most probably a signature of the strong fluctuations. Note that it is not too surprising that near the phase boundary, the methods may produce different outcomes for the order parameter. In the CDW phase, the three methods coincide up to 4 significant digits yielding a finite value of the order parameter, as expected. In particular, the DMRG3S+LBO and PP-2DMRG methods coincide up to a relative precision of 10^{-5} . However, at (P.3) all methods do not agree with respect to their error bounds obtained from the finite-size scaling, which was also found in the ground-state energy extrapolation.

A more careful convergence analysis is essential to achieve consistent extrapolations, which, however, is not the goal of this comparison. Instead, we want to point out that for the case of heavy polarons, ensuring the convergence with respect to all numerical

control parameters is of particular importance.

4. Conclusion

We discussed three state-of-the-art matrix-product-state methods to simulate numerically challenging systems with large local Hilbert spaces and broken $U(1)$ -symmetries that appear in various physical problem settings [13, 38–48]. The presented methods exploit different representations and optimization schemes to reduce the computational costs. The pseudosite method (PS-DMRG) unfolds the large local Hilbert space into additional sites using a compact binary encoding of the local degrees of freedom. Efficiently representing large local Hilbert spaces by means of the local basis optimization (DMRG3S+LBO) directly operates on the physical degrees of freedom. These are rotated into an optimal basis in which the single-site reduced density matrix is diagonal and can be truncated faithfully. The recently developed projected purification (PP-2DMRG) interpolates between both approaches in the sense that the system is extended by pairing up each lattice site with a bath site, and truncated according to the diagonal elements of the single-site reduced density matrix.

Being conceptually very different, it is not immediately clear which method is best suited for a given problem setting. For that reason, we applied these methods to the Holstein model at half filling, which is a prototypical system featuring Einstein phonons with large local Hilbert spaces and broken $U(1)$ -symmetries. We performed two different common numerical analyses: a high-precision scaling analysis of the model’s ground-state energy as a function of the maximally allowed bond dimension at an intermediate system size ($L = 51$ sites) as well as finite-size extrapolations for intensive quantities such as the CDW order parameter in the ground state up to systems with $L = 201$ sites. Our comparisons demonstrate that, in general, all methods characterize the different phases with high numerical precision and allow for an extrapolation of observables towards the thermodynamic limit. It should be noted that both PS-DMRG and PP-2DMRG require fewer modifications to an existing code compared to an implementation of DMRG3S+LBO. In particular, PS-DMRG can be readily used if the implementation supports combined fermionic and hardcore-bosonic lattice degrees of freedom. In order to use PP-2DMRG, the most relevant required modification is the implementation of the balancing operators which, however, are only local operators, i.e., they can be realized straightforward.

Analyzing the different methods in more detail, we also identify situations in which it can be beneficial to use a particular method. For instance, in the case of broadly distributed phonon-excitation probabilities, the DMRG3S+LBO and PP-2DMRG methods benefit from their capability of truncations on the phononic degrees of freedom. Here, in particular, the DMRG3S+LBO method achieves very compact representations with the smallest bond dimensions found in our calculations (figures 12 to 14). This comes at the cost of a larger amount of numerical control parameters such as the number of phonons per lattice site in combination with the amount of optimal modes

kept, or the mixing factor used in the ground-state search. As discussed in section 2.3.3, using improper configurations can produce a strong dependency on the initial state, which becomes particularly important in the CDW phase, where heavy polarons slow down the overall convergence of the ground-state search. In these situations, the 2-site solvers used in the PS-DMRG and PP-2DMRG methods together with the fact that the only relevant control parameter is the maximum bond dimension seem to be easier to control. Finally, it should be pointed out that PP-2DMRG is capable of exploiting restored global $U(1)$ symmetries, which reduces computational costs associated with the local degrees of freedom. Therefore, even though larger maximal bond dimensions are required to achieve the same numerical precision as the PS-DMRG and DMRG3S+LBO methods, this is compensated by the more efficient representation of matrix-product states and operators as can be seen in figures 12 and 14 where the most accurate ground-state approximations are found by PP-2DMRG. However, since the maximally allowed bond dimension is limited to $m_{\max} \leq 2000$ in our calculations, close to the phase boundary, the more compact representation of DMRG3S+LBO yields the best approximation (see figure 13).

Another important aspect is the question of the applicability of the described methods to study out-of-equilibrium setups. The DMRG-LBO already proved its capability to simulate the dynamics of systems with small fermion densities coupled to lattice phonons [26, 81], global quenches [27, 30] and also finite-temperature simulations [82] by using a Trotter decomposition of the time-evolution operator. A very natural, further development would be to employ time-evolution schemes such as the time-dependent variational principle (TDVP) [83, 84] or the W^{II} -representation [85] for time-evolution allowing the efficient treatment of long-ranged interactions and larger time-steps (TDVP). From our previous discussion, we expect the DMRG-LBO as well as the projected purification to be well-suited for an adoption of TDVP as the time-evolution scheme (see [86] for developments to combine LBO with TDVP), while due to the continuously required basis transformations of the Hamiltonian, the W^{II} method seems to be more suitable for the projected purification.

5. Acknowledgments

We thank K. Harms and D. Jansen for insightful discussions. TK acknowledges financial support by the ERC Starting Grant from the European Union’s Horizon 2020 research and innovation program under grant agreement No. 758935. This work was funded by the Deutsche Forschungsgemeinschaft (DFG, German Research Foundation) – 207383564; 217133147, via FOR 1807 (projects P4 and P7) and CRC 1073 (projects B03 and B09), respectively. SP acknowledges support by the Deutsche Forschungsgemeinschaft (DFG, German Research Foundation) under Germany’s Excellence Strategy-426 EXC-2111-390814868. We thank the TU Clausthal for providing access to the Nuku computational cluster.

References

- [1] White S R 1992 *Phys. Rev. Lett.* **69** 2863–2866 URL <https://journals.aps.org/prl/abstract/10.1103/PhysRevLett.69.2863>
- [2] White S R 1993 *Phys. Rev. B* **48** 10345–10356 URL <https://link.aps.org/doi/10.1103/PhysRevB.48.10345>
- [3] Östlund S and Rommer S 1995 *Phys. Rev. Lett.* **75**(19) 3537–3540 URL <http://link.aps.org/doi/10.1103/PhysRevLett.75.3537>
- [4] Vidal G 2004 *Phys. Rev. Lett.* **93**(4) 040502 URL <http://link.aps.org/doi/10.1103/PhysRevLett.93.040502>
- [5] Verstraete F and Cirac J I 2006 *Phys. Rev. B* **73**(9) 094423 URL <https://link.aps.org/doi/10.1103/PhysRevB.73.094423>
- [6] Schollwöck U 2011 *Annals of Physics* **326** 96 – 192 ISSN 0003-4916 january 2011 Special Issue URL <http://www.sciencedirect.com/science/article/pii/S0003491610001752>
- [7] Paeckel S, Köhler T, Swoboda A, Manmana S R, Schollwöck U and Hubig C 2019 *Annals of Physics* **411** 167998 ISSN 0003-4916 URL <http://dx.doi.org/10.1016/j.aop.2019.167998>
- [8] Verstraete F, Porras D and Cirac J I 2004 *Phys. Rev. Lett.* **93**(22) 227205 URL <https://link.aps.org/doi/10.1103/PhysRevLett.93.227205>
- [9] Verstraete F, Murg V and Cirac J 2008 *Advances in Physics* **57** 143–224 URL <https://doi.org/10.1080/14789940801912366>
- [10] Schuch N, Wolf M M, Verstraete F and Cirac J I 2008 *Phys. Rev. Lett.* **100**(4) 040501 URL <https://link.aps.org/doi/10.1103/PhysRevLett.100.040501>
- [11] Vidal G 2007 *Phys. Rev. Lett.* **99**(22) 220405 URL <https://link.aps.org/doi/10.1103/PhysRevLett.99.220405>
- [12] Orús R 2014 *The European Physical Journal B* **87** ISSN 1434-6036 URL <http://dx.doi.org/10.1140/epjb/e2014-50502-9>
- [13] Holstein T 1959 *Ann. Phys.* **8** 325–342 ISSN 0003-4916 URL <http://www.sciencedirect.com/science/article/pii/0003491659900028>
- [14] Tezuka M, Arita R and Aoki H 2005 *Phys. Rev. Lett.* **95**(22) 226401 URL <https://link.aps.org/doi/10.1103/PhysRevLett.95.226401>
- [15] Matsueda H and Ishihara S 2007 *Journal of the Physical Society of Japan* **76** 083703 ISSN 1347-4073 URL <http://dx.doi.org/10.1143/JPSJ.76.083703>
- [16] Marsiglio F 1995 *Physica C: Superconductivity* **244** 21 – 34 ISSN 0921-4534 URL <http://www.sciencedirect.com/science/article/pii/0921453495000461>
- [17] Wellein G, Röder H and Fehske H 1996 *Phys. Rev. B* **53**(15) 9666–9675 URL <https://link.aps.org/doi/10.1103/PhysRevB.53.9666>
- [18] Weiße A and Fehske H 1998 *Phys. Rev. B* **58**(20) 13526–13533 URL <https://link.aps.org/doi/10.1103/PhysRevB.58.13526>

- [19] Bonča J, Trugman S A and Batistić I 1999 *Phys. Rev. B* **60**(3) 1633–1642 URL <https://link.aps.org/doi/10.1103/PhysRevB.60.1633>
- [20] Weiße A, Fehske H, Wellein G and Bishop A R 2000 *Phys. Rev. B* **62**(2) R747–R750 URL <https://link.aps.org/doi/10.1103/PhysRevB.62.R747>
- [21] Hohenadler M, Evertz H G and von der Linden W 2004 *Phys. Rev. B* **69**(2) 024301 URL <https://link.aps.org/doi/10.1103/PhysRevB.69.024301>
- [22] Wall M L, Safavi-Naini A and Rey A M 2016 *Phys. Rev. A* **94**(5) 053637 URL <https://link.aps.org/doi/10.1103/PhysRevA.94.053637>
- [23] Jeckelmann E and White S R 1998 *Phys. Rev. B* **57**(11) 6376–6385 URL <https://link.aps.org/doi/10.1103/PhysRevB.57.6376>
- [24] Loos J, Hohenadler M, Alvermann A and Fehske H 2006 *Journal of Physics: Condensed Matter* **18** 7299–7312 ISSN 1361-648X URL <http://dx.doi.org/10.1088/0953-8984/18/31/023>
- [25] Heidrich-Meisner F, Feiguin A E and Dagotto E 2009 *Phys. Rev. B* **79** 235336 URL <https://journals.aps.org/prb/abstract/10.1103/PhysRevB.79.235336>
- [26] Brockt C, Dorfner F, Vidmar L, Heidrich-Meisner F and Jeckelmann E 2015 *Phys. Rev. B* **92**(24) 241106 URL <https://link.aps.org/doi/10.1103/PhysRevB.92.241106>
- [27] Hashimoto H and Ishihara S 2017 *Phys. Rev. B* **96**(3) 035154 URL <https://link.aps.org/doi/10.1103/PhysRevB.96.035154>
- [28] Weber M, Assaad F F and Hohenadler M 2018 *Phys. Rev. B* **98**(23) 235117 URL <https://link.aps.org/doi/10.1103/PhysRevB.98.235117>
- [29] Kloss B, Reichman D R and Tempelaar R 2019 *Phys. Rev. Lett.* **123**(12) 126601 URL <https://link.aps.org/doi/10.1103/PhysRevLett.123.126601>
- [30] Stolpp J, Herbrych J, Dorfner F, Dagotto E and Heidrich-Meisner F 2020 *Phys. Rev. B* **101**(3) 035134 URL <https://link.aps.org/doi/10.1103/PhysRevB.101.035134>
- [31] Jeckelmann E and Fehske H 2007 *Riv. Nuovo Cimento* **30** 259–292 URL <https://www.sif.it/riviste/sif/ncr/econtents/2007/030/06/article/0>
- [32] Weiße A and Fehske H 2008 *Exact Diagonalization Techniques* (Berlin, Heidelberg: Springer Berlin Heidelberg) pp 529–544 ISBN 978-3-540-74686-7 URL https://doi.org/10.1007/978-3-540-74686-7_18
- [33] Assaad F and Evertz H 2008 *World-line and Determinantal Quantum Monte Carlo Methods for Spins, Phonons and Electrons* (Berlin, Heidelberg: Springer Berlin Heidelberg) pp 277–356 ISBN 978-3-540-74686-7 URL https://doi.org/10.1007/978-3-540-74686-7_10
- [34] Hohenadler M and Lang T C 2008 *Autocorrelations in Quantum Monte Carlo Simulations of Electron-Phonon Models* (Berlin, Heidelberg: Springer Berlin Heidelberg) pp 357–366 ISBN 978-3-540-74686-7 URL https://doi.org/10.1007/978-3-540-74686-7_11

- [35] Werner P and Millis A J 2007 *Phys. Rev. Lett.* **99**(14) 146404 URL <https://link.aps.org/doi/10.1103/PhysRevLett.99.146404>
- [36] Aoki H, Tsuji N, Eckstein M, Kollar M, Oka T and Werner P 2014 *Rev. Mod. Phys.* **86**(2) 779–837 URL <https://link.aps.org/doi/10.1103/RevModPhys.86.779>
- [37] Kemper A F, Sentef M A, Moritz B, Devereaux T P and Fredericks J K 2017 *Annalen der Physik* **529** 1600235 (*Preprint* <https://onlinelibrary.wiley.com/doi/pdf/10.1002/andp.201600235>) URL <https://onlinelibrary.wiley.com/doi/abs/10.1002/andp.201600235>
- [38] Bloch I 2005 *Nat Phys* **1** 23–30 URL <https://doi.org/10.1038/nphys138>
- [39] Heidrich-Meisner F, Feiguin A E, Schollwöck U and Zwerger W 2010 *Phys. Rev. A* **81**(2) 023629 URL <https://link.aps.org/doi/10.1103/PhysRevA.81.023629>
- [40] Ejima S, Bhaseen M J, Hohenadler M, Essler F H L, Fehske H and Simons B D 2011 *Phys. Rev. Lett.* **106**(1) 015303 URL <https://link.aps.org/doi/10.1103/PhysRevLett.106.015303>
- [41] Dorfner F and Heidrich-Meisner F 2016 *Phys. Rev. A* **93**(6) 063624 URL <https://link.aps.org/doi/10.1103/PhysRevA.93.063624>
- [42] Purdy T P, Brooks D W C, Botter T, Brahms N, Ma Z Y and Stamper-Kurn D M 2010 *Phys. Rev. Lett.* **105**(13) 133602 URL <https://link.aps.org/doi/10.1103/PhysRevLett.105.133602>
- [43] Thompson J D, Tiecke T G, de Leon N P, Feist J, Akimov A V, Gullans M, Zibrov A S, Vuletić V and Lukin M D 2013 *Science* **340** 1202–1205 ISSN 0036-8075 URL <https://science.sciencemag.org/content/340/6137/1202>
- [44] Ritsch H, Domokos P, Brennecke F and Esslinger T 2013 *Rev. Mod. Phys.* **85**(2) 553–601 URL <https://link.aps.org/doi/10.1103/RevModPhys.85.553>
- [45] Brouwer P W, Duckheim M, Romito A and von Oppen F 2011 *Phys. Rev. B* **84**(14) 144526 URL <https://link.aps.org/doi/10.1103/PhysRevB.84.144526>
- [46] Cook A and Franz M 2011 *Phys. Rev. B* **84**(20) 201105 URL <https://link.aps.org/doi/10.1103/PhysRevB.84.201105>
- [47] Hui H Y, Brydon P M R, Sau J D, Tewari S and Sarma S D 2015 *Scientific Reports* **5** 8880 URL <https://doi.org/10.1038/srep08880>
- [48] Keselman A, Murthy C, van Heck B and Bauer B 2019 *SciPost Phys.* **7**(4) 50 URL <https://scipost.org/10.21468/SciPostPhys.7.4.050>
- [49] Zhang C, Jeckelmann E and White S R 1998 *Phys. Rev. Lett.* **80**(12) 2661–2664 URL <https://link.aps.org/doi/10.1103/PhysRevLett.80.2661>
- [50] Bursill R J 1999 *Phys. Rev. B* **60**(3) 1643–1649 URL <https://link.aps.org/doi/10.1103/PhysRevB.60.1643>
- [51] Friedman B 2000 *Phys. Rev. B* **61**(10) 6701–6705 URL <https://link.aps.org/doi/10.1103/PhysRevB.61.6701>

- [52] Wong H and Chen Z D 2008 *Phys. Rev. B* **77**(17) 174305 URL <https://link.aps.org/doi/10.1103/PhysRevB.77.174305>
- [53] Köhler T, Stolpp J and Paeckel S 2020 Efficient and flexible approach to simulate low-dimensional quantum lattice models with large local Hilbert spaces (*Preprint* 2008.08466) URL <https://arxiv.org/abs/2008.08466>
- [54] Hirsch J E and Fradkin E 1983 *Phys. Rev. B* **27**(7) 4302–4316 URL <https://link.aps.org/doi/10.1103/PhysRevB.27.4302>
- [55] Bursill R J, McKenzie R H and Hamer C J 1998 *Phys. Rev. Lett.* **80**(25) 5607–5610 URL <https://link.aps.org/doi/10.1103/PhysRevLett.80.5607>
- [56] Creffield C E, Sangiovanni G and Capone M 2005 *The European Physical Journal B - Condensed Matter and Complex Systems* **44** 175–181 URL <https://doi.org/10.1140/epjb/e2005-00112-9>
- [57] Jeckelmann E, Zhang C and White S R 1999 *Phys. Rev. B* **60**(11) 7950–7955 URL <https://link.aps.org/doi/10.1103/PhysRevB.60.7950>
- [58] McCulloch I P 2007 *Journal of Statistical Mechanics: Theory and Experiment* **2007** P10014 URL <http://stacks.iop.org/1742-5468/2007/i=10/a=P10014>
- [59] Singh S, Pfeifer R N C and Vidal G 2010 *Phys. Rev. A* **82**(5) 050301 URL <https://link.aps.org/doi/10.1103/PhysRevA.82.050301>
- [60] Singh S, Pfeifer R N C and Vidal G 2011 *Phys. Rev. B* **83**(11) 115125 URL <https://link.aps.org/doi/10.1103/PhysRevB.83.115125>
- [61] Vidal G 2003 *Phys. Rev. Lett.* **91**(14) 147902 URL <https://link.aps.org/doi/10.1103/PhysRevLett.91.147902>
- [62] Peschel I 2004 *Journal of Statistical Mechanics: Theory and Experiment* **2004** P12005 URL <https://iopscience.iop.org/article/10.1088/1742-5468/2004/12/P12005>
- [63] Calabrese P and Cardy J 2004 *J. Stat. Mech.: Theor. and Exp.* P06002 URL <http://stacks.iop.org/1742-5468/2004/P06002>
- [64] Eisert J, Cramer M and Plenio M B 2010 *Rev. Mod. Phys.* **82**(1) 277–306 URL <https://link.aps.org/doi/10.1103/RevModPhys.82.277>
- [65] Hubig C, McCulloch I P, Schollwöck U and Wolf F A 2015 *Phys. Rev. B* **91**(15) 155115 URL <https://link.aps.org/doi/10.1103/PhysRevB.91.155115>
- [66] Pai R V, Pandit R, Krishnamurthy H R and Ramasesha S 1996 *Phys. Rev. Lett.* **76**(16) 2937–2940 URL <https://link.aps.org/doi/10.1103/PhysRevLett.76.2937>
- [67] Caron L G and Moukouri S 1996 *Phys. Rev. Lett.* **76**(21) 4050–4053 URL <https://link.aps.org/doi/10.1103/PhysRevLett.76.4050>
- [68] Caron L G and Moukouri S 1997 *Phys. Rev. B* **56**(14) R8471–R8474 URL <https://link.aps.org/doi/10.1103/PhysRevB.56.R8471>

- [69] Tezuka M, Arita R and Aoki H 2007 *Phys. Rev. B* **76**(15) 155114 URL <https://link.aps.org/doi/10.1103/PhysRevB.76.155114>
- [70] Fehske H, Hager G and Jeckelmann E 2008 *Europhys. Lett.* **84** 57001 URL <https://iopscience.iop.org/article/10.1209/0295-5075/84/57001>
- [71] Ejima S and Fehske H 2009 *Europhys. Lett.* **87** 27001 URL <https://iopscience.iop.org/article/10.1209/0295-5075/87/27001>
- [72] Dorfner F 2017 *Numerical methods for strongly correlated many-body systems with bosonic degrees of freedom* Ph.D. thesis Ludwig-Maximilians-Universität München URL <http://nbn-resolving.de/urn:nbn:de:bvb:19-205528>
- [73] Guo C, Weichselbaum A, von Delft J and Vojta M 2012 *Phys. Rev. Lett.* **108**(16) 160401 URL <https://link.aps.org/doi/10.1103/PhysRevLett.108.160401>
- [74] Bruognolo B, Weichselbaum A, Guo C, von Delft J, Schneider I and Vojta M 2014 *Phys. Rev. B* **90**(24) 245130 URL <https://link.aps.org/doi/10.1103/PhysRevB.90.245130>
- [75] Blunden-Codd Z, Bera S, Bruognolo B, Linden N O, Chin A W, von Delft J, Nazir A and Florens S 2017 *Phys. Rev. B* **95**(8) 085104 URL <https://link.aps.org/doi/10.1103/PhysRevB.95.085104>
- [76] Bruognolo B, Linden N O, Schwarz F, Lee S S B, Stadler K, Weichselbaum A, Vojta M, Anders F B and von Delft J 2017 *Phys. Rev. B* **95**(12) 121115 URL <https://link.aps.org/doi/10.1103/PhysRevB.95.121115>
- [77] Dorfner F, Vidmar L, Brockt C, Jeckelmann E and Heidrich-Meisner F 2015 *Phys. Rev. B* **91**(10) 104302 URL <http://link.aps.org/doi/10.1103/PhysRevB.91.104302>
- [78] White S R 2005 *Phys. Rev. B* **72**(18) 180403 URL <https://link.aps.org/doi/10.1103/PhysRevB.72.180403>
- [79] Lang I and Firsov Y A 1963 *Sov. Phys. JETP* **16** 1301 URL <http://www.jetp.ac.ru/cgi-bin/e/index/e/16/5/p1301?a=list>
- [80] Hubig C, Haegeman J and Schollwöck U 2018 *Phys. Rev. B* **97**(4) 045125 URL <https://link.aps.org/doi/10.1103/PhysRevB.97.045125>
- [81] Brockt C and Jeckelmann E 2017 *Phys. Rev. B* **95**(6) 064309 URL <https://link.aps.org/doi/10.1103/PhysRevB.95.064309>
- [82] Jansen D, Bonča J and Heidrich-Meisner F 2020 *Phys. Rev. B* **102**(16) 165155 URL <https://link.aps.org/doi/10.1103/PhysRevB.102.165155>
- [83] Haegeman J, Cirac J I, Osborne T J, Pižorn I, Verschelde H and Verstraete F 2011 *Phys. Rev. Lett.* **107**(7) 070601 URL <https://link.aps.org/doi/10.1103/PhysRevLett.107.070601>
- [84] Haegeman J, Lubich C, Oseledets I, Vandereycken B and Verstraete F 2016 *Phys. Rev. B* **94**(16) 165116 URL <https://link.aps.org/doi/10.1103/PhysRevB.94.165116>

- [85] Zaletel M P, Mong R S K, Karrasch C, Moore J E and Pollmann F 2015 *Phys. Rev. B* **91**(16) 165112 URL <https://link.aps.org/doi/10.1103/PhysRevB.91.165112>
- [86] Schröder F A Y N and Chin A W 2016 *Phys. Rev. B* **93**(7) 075105 URL <https://link.aps.org/doi/10.1103/PhysRevB.93.075105>